Chemistry and microbiology of the Critical Zone along a steep climate and vegetation gradient in the Chilean Coastal Cordillera

Ralf A. Oeser[a,*], Nicole Stroncik[a,d], Lisa-Marie Moskwa[b], Nadine Bernhard[e], Mirjam Schaller[f], Rafaella Canessa[g], Liesbeth van den Brink[h], Moritz Köster[i], Emanuel Brucker[j], Svenja Stock[k], Juan Pablo Fuentes[l], Roberto Godoy[m], Francisco Javier Matus[n], Rómulo Oses Pedraza[o,p], Pablo Osses McIntyre[q], Leandro Paulino[r], Oscar Seguel[s], Maaike Y. Bader[g], Jens Boy[t], Michaela A. Dippold[i], Todd A. Ehlers[f], Peter Kühn[e], Yakov Kuzyakov[k], Peter Leinweber[u], Thomas Scholten[e], Sandra Spielvogel[v], Marie Spohn[j], Kirstin Übernickel[f], Katja Tielbörger[h], Dirk Wagner[b,w], Friedhelm von Blanckenburg[a,c]

[a] GFZ German Research Centre for Geosciences, Section 3.3 Earth Surface Geochemistry, Telegrafenberg, D-14473 Potsdam, Germany
[b] GFZ German Research Centre for Geosciences, Section 5.3 Geomicrobiology, Telegrafenberg, D-14473 Potsdam, Germany
[c] Freie Universität Berlin; Institute of Geological Science, Malteserstr. 74-100, Building N, D-12249 Berlin, Germany
[d] GFZ German Research Centre for Geosciences, Section 3.1 Inorganic and Isotope Geochemistry, Telegrafenberg, D-14473 Potsdam, Germany
[e] University of Tübingen, Soil Science and Geomorphology, Rümelinstraße 19-23, D-72070 Tübingen, Germany
[f] University of Tübingen, Department of Geosciences, Wilhelmstraße 56, D-72074 Tübingen, Germany
[g] Philipps-University Marburg, Ecological Plant Geography, Deutschhausstraße 10, D-35032 Marburg, Germany
[h] University of Tübingen, Plant Ecology, Auf der Morgenstelle 5, D-72076 Tübingen, Germany
[i] Georg-August-University Göttingen, Biogeochemistry of Agroecosystems, Büsgenweg 2, D-37077 Göttingen, Germany
[j] University of Bayreuth, Institute of Soil Ecology, Dr.-Hans-Frisch-Straße 1-3, D-95448 Bayreuth, Germany
[k] Georg-August-University Göttingen, Soil Science of Temperate Ecosystems, Büsgenweg 2, D-37077 Göttingen, Germany
[l] Universidad de Chile, Facultad de Ciencias Forestales y de la Conservación de la Naturaleza, Av. Santa Rosa, 11315 La Pintana, Santiago, Chile
[m] Universidad Austral de Chile, Instituto de Ciencias Ambientales y Evolutivas, Avenida Eduardo Morales Miranda, Campus Isla Teja, Valdivia, Chile
[n] Universidad de La Frontera, Departamento de Ciencias Químicas y Recursos Naturales, Scientific and Technological Bioresource Nucleus (BIOREN-UFRO), Temuco, Chile
[o] Centro de Estudios Avanzados en Zonas Aridas (CEAZA), Raúl Britán #1305, Campus Andrés Bello Universidad de La Serena, La Serena, Chile
[p] Universidad de Atacama, CRIDESAT, Copayapu 484, Copaipó, Chile
[q] Pontificia Universidad Católica de Chile, Instituto de Geografía, Vicuña Mackenna 4860, Macul, Santiago, Chile
[r] Universidad de Concepción, Departamento de Suelos y Recursos Naturales, Facultad de Agronomía, Avda. Vicente Méndez 595, Chillán, Chile
[s] Universidad de Chile, Facultad de Ciencias Agronómicas, Av. Santa Rosa #11315, 8820808 La Pintana, Santiago, Chile
[t] Leibniz University Hannover, Institute of Soil Science, Herrenhäuser Straße 2, D-30419 Hannover, Germany
[u] University of Rostock, Faculty of Agricultural and Environmental Sciences, Soil Science, Justus-von-Liebig-Weg 6, D-18059 Rostock, Germany
[v] Christian-Albrechts-University Kiel, Institute of Soil Science, Herman-Rodewald-Straße 2, D-24118 Kiel, Germany
[w] University of Potsdam, Institute of Earth and Environmental Science, Karl-Liebknecht-Strasse 24-25, 14476 Potsdam, Germany

ARTICLE INFO

ABSTRACT

The Chilean Coastal Cordillera features a spectacular climate and vegetation gradient, ranging from arid and unvegetated areas in the north to humid and forested areas in the south. The EarthShape project ("*Earth Surface Shaping by Biota*") uses this natural gradient to investigate how climate and biological processes shape the Earth's surface. We explored the Critical Zone, the Earth's uppermost layer, in four key sites located in desert, semi-desert, Mediterranean, and temperate climate zones of the Coastal Cordillera, with the focus on weathering of granitic rock. Here, we present first results from 16 approximately 2 m-deep regolith profiles to document: (1)

architecture of weathering zone; (2) degree and rate of rock weathering, thus the release of mineral-derived nutrients to the terrestrial ecosystems; (3) denudation rates; and (4) microbial abundances of bacteria and archaea in the saprolite.

From north to south, denudation rates from cosmogenic nuclides are $\sim 10\,t\,km^{-2}\,yr^{-1}$ at the arid Pan de Azúcar site, $\sim 20\,t\,km^{-2}\,yr^{-1}$ at the semi-arid site of Santa Gracia, $\sim 60\,t\,km^{-2}\,yr^{-1}$ at the Mediterranean climate site of La Campana, and $\sim 30\,t\,km^{-2}\,yr^{-1}$ at the humid site of Nahuelbuta. A and B horizons increase in thickness and elemental depletion or enrichment increases from north ($\sim 26°S$) to south ($\sim 38°S$) in these horizons. Differences in the degree of chemical weathering, quantified by the chemical depletion fraction (CDF), are significant only between the arid and sparsely vegetated site and the other three sites. Differences in the CDF between the sites, and elemental depletion within the sites are sometimes smaller than the variations induced by the bedrock heterogeneity. Microbial abundances (bacteria and archaea) in saprolite substantially increase from the arid to the semi-arid sites.

With this study, we provide a comprehensive dataset characterizing the Critical Zone geochemistry in the Chilean Coastal Cordillera. This dataset confirms climatic controls on weathering and denudation rates and provides prerequisites to quantify the role of biota in future studies.

1. Introduction

The Earth's surface, where rock, the atmosphere, the hydrosphere, and the biosphere interact, is often referred to as the Critical Zone (Anderson et al., 2007). Soils, mantling 95% of the terrestrial Earth's surface, are the top layer of this zone. Soil is made "from below" by weathering, the breakdown of rocks and minerals (Riebe et al., 2017), and "from above" by the addition of organic matter and atmospheric inputs (Chorover et al., 2007). Weathering turns fresh rock into a loosely consolidated "regolith" (comprising both mobile soil at the top and weathered rock beneath it). The inorganic chemical process of weathering involves the dissolution of primary minerals and their partitioning into solutes and secondary minerals (e.g. amorphous and crystalline oxides, clays). These abiotic weathering products, as well as organic compounds, are exported from catchments via erosion and rivers (Gaillardet et al., 1999; Hilton, 2017). The Critical Zone thus plays an important role in the cycling of mineral nutrients across the Earth's surface and the mechanisms of weathering are key.

Numerous studies have shown that soil physico-chemical parameters, such as soil organic matter, soil acidity, exchangeable ions, extractable oxides, and volumetric strain (ε) systematically change with temperature and precipitation (e.g. Bardelli et al., 2017; Bojko and Kabala, 2017; Khomo et al., 2013; Khomo et al., 2011; Khormali et al., 2012). Egli et al. (2003) have shown that the amount of smectite and the degree of weathering in Alpine soils increase with precipitation. Moreover, the degree of plagioclase weathering seems to increase exponentially with temperature and linearly with precipitation (Dere et al., 2013). Still, from studies that make use of climatic gradients no clear relationship between climate and denudation rates has yet emerged. Large variations in denudation rates in any given climate indicate that a potential climatic imprint might have been severely overprinted by factors such as uplift, physical and chemical bedrock characteristics, and biota (e.g. Dixon et al., 2009; Egli et al., 2004; Ferrier et al., 2012; Riebe et al., 2004; Schaller et al., 2018; Starke et al., 2017). In this context, Owen et al. (2011) postulated that a mean annual precipitation threshold exists below which bedrock denudation is precipitation-dependent and above which soil production from bedrock is controlled by complex feedback mechanisms between tectonics, temperature, and biota.

One of the key players in weathering processes is biota, which is receiving increasing scientific attention in this context (Amundson et al., 2015b; Brantley et al., 2011; Egli et al., 2014; Hahm et al., 2014). A broad spectrum of biota (plants, animals, and microorganisms) interacts with the Earth's surface, although the direction and magnitude of the effects biota has on Earth-surface processes, and conversely the Earth surface effects on biota, are still not well understood (e.g. Wilcke et al., 2017). For example, little is known about microorganisms that live beneath soil, even though more than one third of the microbial biomass is concentrated in regolith depths deeper than 25 cm (Fierer

et al., 2003; Schutz et al., 2010). Several studies demonstrated that even in the saprolite active bacterial cells exist (Buss et al., 2005; Richter and Markewitz, 1995). Biogenic weathering is a potentially important mechanism because microorganisms in the regolith are highly specialized to their environment (Fritze et al., 2000; Ghiorse and Wilson, 1988; Zvyagintsev, 1994). Fungi and their associated bacteria can directly weather minerals (Balogh-Brunstad et al., 2008; Quirk et al., 2014; Smits et al., 2012). In this process they mobilize mineral-bound nutrients (e.g. P, Ca, Mg, K) that are essential elements to plants. When these nutrients are made available for plants, a biogeochemical cycle is induced that, for some elements, exceeds the weathering flux measured in rivers up to a factor of 40 and more (e.g. Uhlig et al., 2017; Wilcke et al., 2017). This biotically modulated silicate weathering is of major significance for global atmospheric CO_2 cycles in the Phanerozoic (Doughty et al., 2014; Pagani et al., 2009; Quirk et al., 2012) and for sustaining a continuous soil cover (Amundson et al., 2015a). Whether these biological mechanisms overwhelm the abiotic weathering mechanisms and whether they serve to provide a feedback balancing soil erosion and soil production have never been shown, owing to the lack of diagnostic observables that allow distinguishing between abiotic and biotic drivers.

To resolve the control of climate and biota on rock disintegration, we combined the fields of geochemistry, soil science, biogeochemistry, and geomorphology and applied these to different study sites along the Chilean Coastal Cordillera. We did this within the German-funded "EarthShape" (Earth surface shaping by biota) research priority program along four Critical Zone field sites along a latitudinal transect in the Chilean Coastal Cordillera. The Coastal Cordillera of Chile encompasses a prominent climate and vegetation gradient that provides a natural laboratory for investigating biotic and abiotic weathering processes. Soil formation processes in this region were previously explored by Owen et al. (2011). The authors found a 40-fold increase in soil production rate from $1\,m\,My^{-1}$ in the hyper-arid to $40\,m\,My^{-1}$ in the arid region. Vázquez et al. (2016) described a > 30 m thick weathering profile developed on granitic bedrock in the Coastal Cordillera in the Mediterranean climate of central Chile. The authors calculated denudation rates (derived from cosmogenic ^{10}Be) from 20 to $70\,m\,My^{-1}$, leading to mean residence times of 0.5 to 1.8 Ma for minerals in the saprolite.

The investigated areas of this study include (from north to south) the Pan de Azúcar National Park ($\sim 26°S$), Santa Gracia Nature Reserve ($\sim 30°S$), La Campana National Park ($\sim 33°S$), and Nahuelbuta National Park ($\sim 38°S$). Site selection for these areas was based on the minimal tectonic and lithologic differences, and their position along the climate (arid to humid) gradient. We thus followed the "climosequence" approach (e.g. Egli et al., 2003). In each of these four study sites, four regolith profiles were excavated on different slope positions.

In this paper, we (1) describe the architecture of the weathering zone; and quantify (2) the degree and rate of rock weathering, thus the

release of mineral-derived nutrients to the terrestrial ecosystems; (3) denudation rates from cosmogenic nuclides; and (4) microbial abundances of bacteria and archaea in the saprolite. We discuss these results on (1) a continental scale, on which the observed geochemical signatures are mainly caused by large scale variations in precipitation and vegetation cover, on (2) a hillslope scale, where influences on weathering and microbial abundances are caused by differing solar irradiation on N- and S-facing slopes, and on (3) a regolith profile scale. Within the scope of the "EarthShape" research program, we thus contribute towards addressing the question: how does the gradient in precipitation and vegetation cover influence weathering, microbial abundances, and mineral nutrient supply to ecosystems? In a companion paper (Bernhard et al., 2018) the site-specific characterization of the soil and its properties are described. With these two papers, we also provide the basic Critical Zone background data that will serve as basis for future studies employing other field and laboratory techniques to decipher the role of biota along this transect.

2. Study area

2.1. Geological and climatic conditions

Central Chile (~25–40˚S) is built of three structural units (from West to East): The Coastal Cordillera, the Central Depression, and the Pre-Western Cordillera of the Andes. Of these, the Coastal Cordillera is the oldest and westernmost trench-parallel morpho-structural unit. The Coastal Cordillera is composed of the remnants of a Late Paleozoic to Mesozoic magmatic arc and Paleozoic metamorphic rocks (Charrier et al., 2007; Hervé et al., 2007; Hervé et al., 1988; Pankhurst and Hervé, 2007; Parada et al., 1988; Vázquez et al., 2016). The northern Coastal Cordillera (~21–27˚S) is suggested to have experienced exhumation between ~118–152 Ma and 60–80 Ma prior to Andean mountain building (Juez-Larré et al., 2010). Following this (from ~40 Ma to present), deformation migrated to the east of the Coastal Cordillera and led to the onset of Andes mountain building and plateau formation (Barnes and Ehlers, 2009). Less well known is the tectonic history of the Coastal Cordillera south of 27˚S, although it is commonly assumed to be similar to the northern Cordillera. More recently, ongoing and minor amounts of Quaternary neotectonic activity have been documented in the northern Coastal Cordillera (Riquelme et al., 2003; Starke et al., 2017).

The EarthShape study area features a vegetation gradient controlled by climate, ranging over 1300 km (from 26˚06′S to 37˚48′S), spanning from arid, via Mediterranean, to humid-temperate climate conditions. Within this area four different sites were chosen, all located within 80 km of the Pacific coast and within plutonic rocks of the Chilean Coastal Cordillera (Fig. 1). The basement at those four sites is mainly composed of: (1) monzo- to syenogranitic intrusions (Pan de Azúcar, Triassic age; Parada et al., 2007), (2) pyroxene and hornblende-bearing diorites and monzodiorites (Santa Gracia granite, 98–89 Ma; Moscoso et al., 1982), and (3), (4) tonalites and granodiorites (Nahuelbuta complex, 294 Ma; Parada et al., 2007 and the Illapel Plutonic Complex in La Campana, 130–90 Ma; Parada et al., 1999).

The 30-year mean annual precipitation (MAP) at the study sites increases from north to south, from $10 \, mm \, yr^{-1}$ in Pan de Azúcar, $89 \, mm \, yr^{-1}$ in Santa Gracia, $436 \, mm \, yr^{-1}$ in La Campana, to $1084 \, mm \, yr^{-1}$ in Nahuelbuta, respectively (Fig. 2a; Ministerio de Obras Públicas, 2017). The mean annual air temperatures (MAT) vary between 18.1 ˚C in the northernmost site and 14.1 ˚C in the southernmost site (Fig. 2b; Ministerio de Obras Públicas, 2017). The northernmost site, Pan de Azúcar, is located at the southern border of the Atacama Desert. The aridity of the Atacama Desert has developed in the Miocene (Clarke, 2006; Dunai et al., 2005), and the hyperaridity in the early Quaternary (Jungers et al., 2013). The sites were unglaciated during the last glacial maximum (Hulton et al., 2002) and are situated in national parks and nature reserves, where anthropogenic influence is minimized
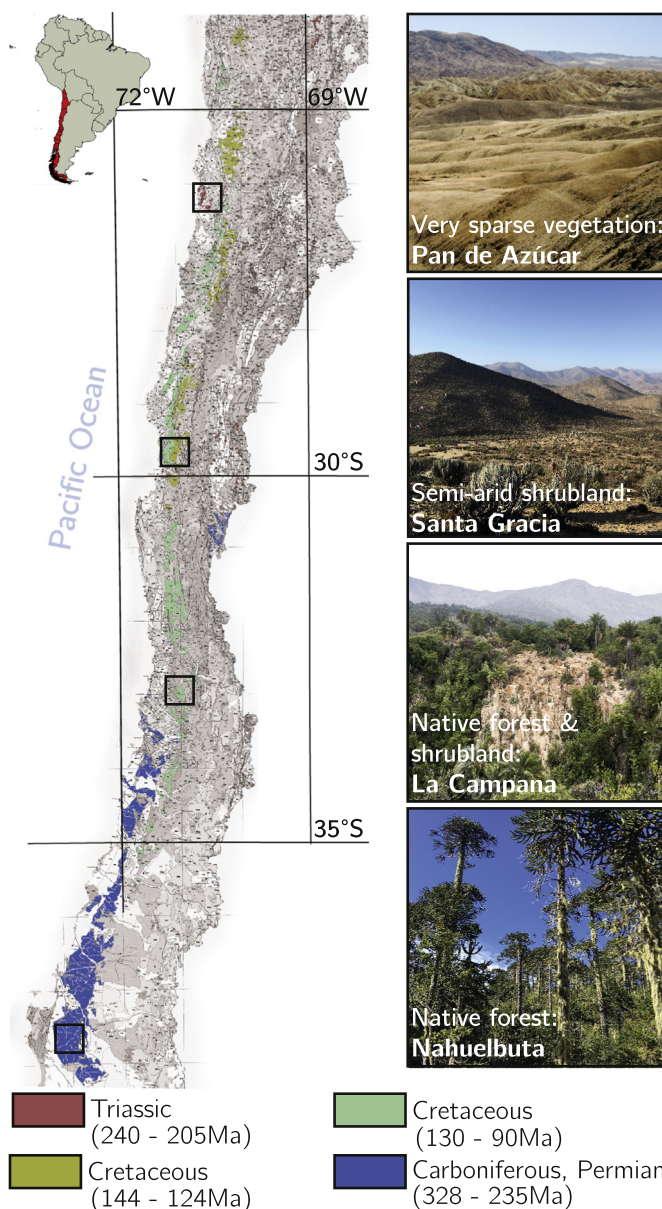
Fig. 1. Intrusion age and spatial extension of the granitoid rocks in the four primary EarthShape study sites (open squares) along the Chilean Coastal Cordillera from north to south: Pan de Azúcar, Santa Gracia, La Campana, and Nahuelbuta.
(Map modified from SERNAGEOMIN, 2003.)

compared to the surrounding areas. However, occasional grazing by cows (La Campana; Rundel and Weisser, 1975) and goats (Santa Gracia; Armesto et al., 2007; Bahre, 1979) within the protected areas have been reported by local authorities.

2.2. Critical Zone description

In each study site, three south-facing (S-facing) profiles at top-, mid-, and toe-slope position and, as an initial cross-check for aspect, a single north-facing (N-facing) mid-slope regolith profile were investigated (Figs. 3–6; Table S1).

Here, we describe the soil as consisting of the O, A, and B horizon, underlain by a C horizon consisting of saprolite (bedrock that was weathered in situ). In this paper, we call the entire zone above unweathered bedrock "regolith" (Scott and Pain, 2008), which thus comprises saprolite and soil. The vascular flora of each study site was
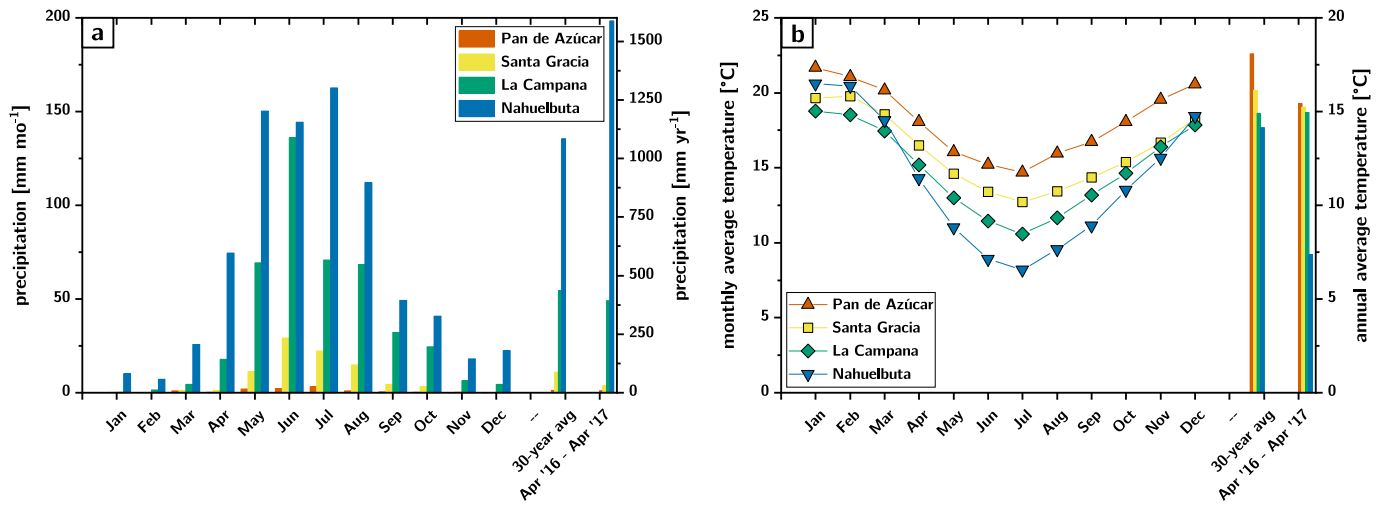
Fig. 2. Compilation of precipitation (A) and temperature (B) data from climate stations in vicinity of the respective EarthShape study sites (Ministerio de Obras Públicas, 2017). Bars on the very right-hand side of both panels show climate data from April 16 to April 17 at the EarthShape climate stations within the study sites (Ehlers et al., 2017).
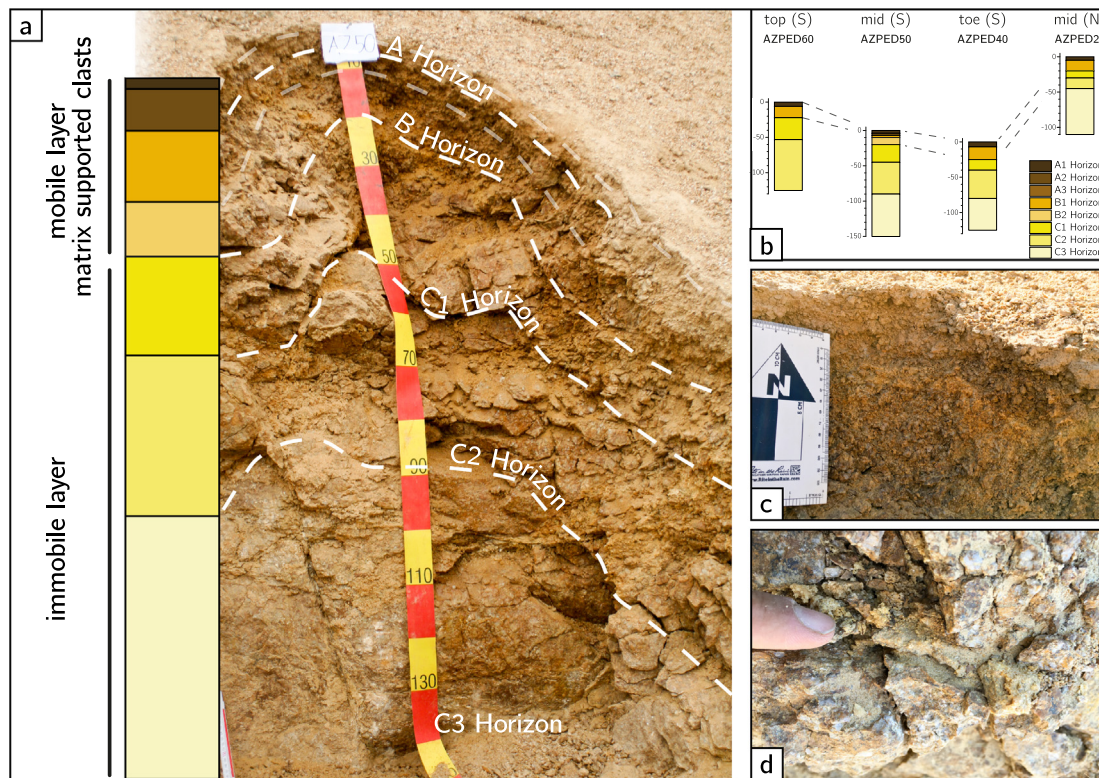
Fig. 3. Photographs of the S-facing mid slope regolith profile (AZPED 50) in Parque Nacional Pan de Azúcar (AZ) including horizon boundaries (white dashed line), a schematic depth profile (a), a cross section through the S-facing catena and adjacent N-facing regolith profile (b). The regolith in AZ developed on a coarse-grained, feldspar-rich granite. Its cover lacks fine-grained particles which are removed by wind (c). Fractures are either filled with clay-sized particles of unknown composition or gypsum and carbonate (d).

classified after Marticorena and Quezada (1985) and Luebert and Pliscoff (2006).

2.2.1. Pan de Azúcar

The S-facing regolith profiles in *Pan de Azúcar national park* (AZ) are located on a slope of 9 m length. The N-facing slope is located at a distance of 30 m from the S-facing slope. The elevations range from 328 to 343 m above sea level (a.s.l.) with hillslope angles between 25 and 40° (Fig. 3b; Table S1).

The profiles' surfaces are comprised of fine grained, quartz-rich granite gruss of a few cm in thickness with a grayish to yellow color (Fig. 3c). At the very top of this A horizon, where silt- and clay-sized particles are absent, angular fragments occur in size of up to 1 cm. Below the top layer, a B horizon of reddish-brown color is found. The size of fragments increases downwards. The transition to the saprolite of the C horizon occurs at 20 to 25 cm depth and does neither depend on slope position nor aspect.

The saprolite has a reddish-brown color and is characterized by coarse-grained material (Fig. 3). The entire regolith is jointed, with joint width and joint spacing augmenting with depth. Joints are either
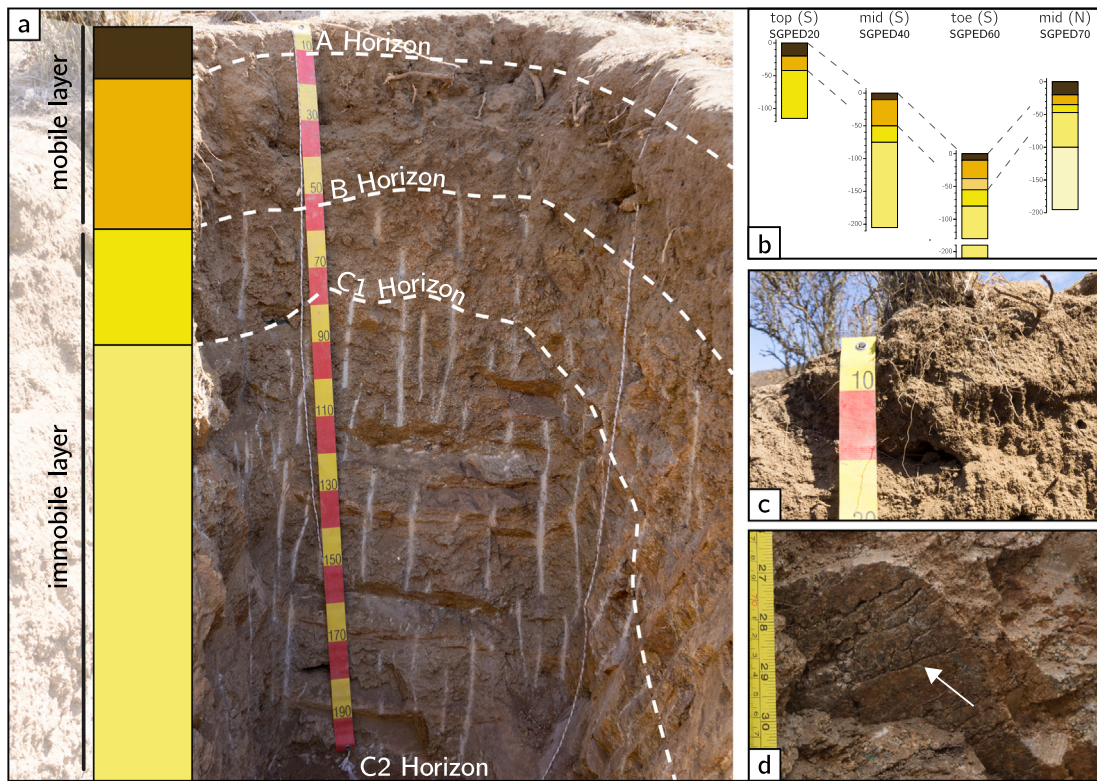
Fig. 4. Photographs of the S-facing mid slope pit (SGPED 40) in Reserva Natural Santa Gracia (SG) including horizon boundaries (white dashed line), a profile sketch, and a cross section through the S-facing catena and adjacent N-facing pit. The catena developed on a medium grain size granitic substrate. The regoliths' upper layer is characterized by bioturbation and a high root density (a). At the pits' base, two major joint sets are preserved. Here, roots penetrate the fractures and weather the adjacent rock face (b).
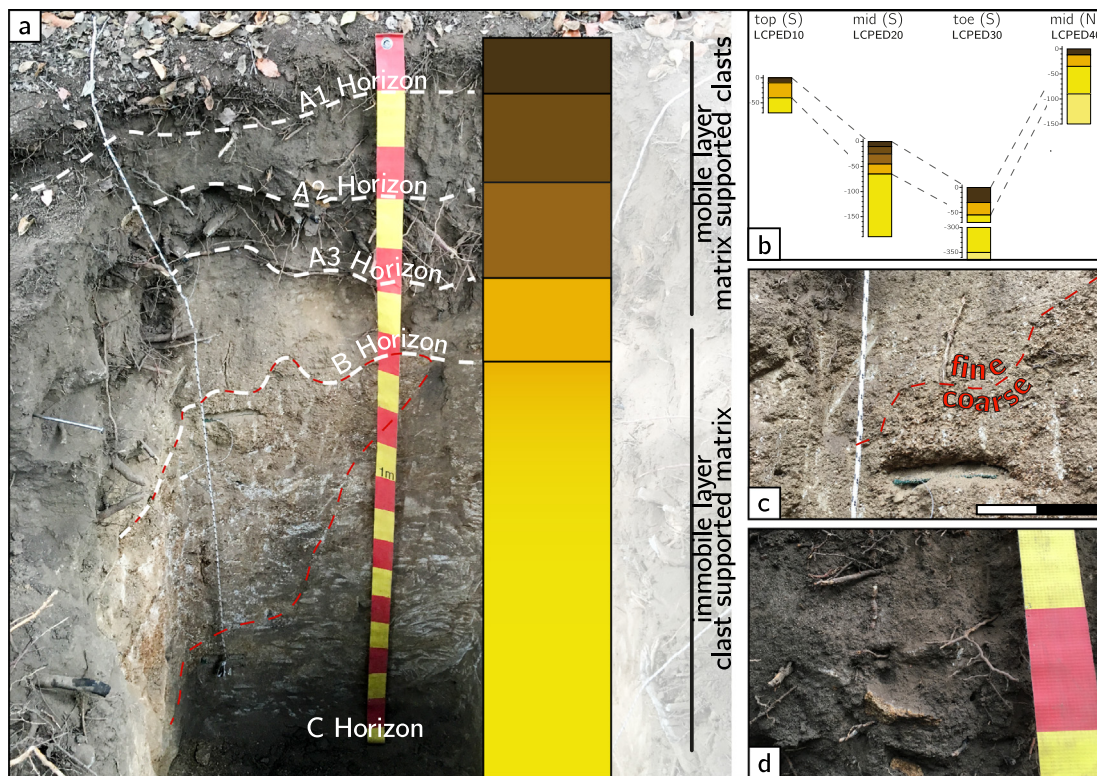
Fig. 5. Photographs of the S-facing mid slope pit (LCPED 20) in Parque Nacional La Campana (LC) including horizon boundaries (white dashed line), a profile sketch, and a cross section through the S-facing catena and adjacent N-facing pit. Both coarse- and fine-grained granodiorite comprise the substrate of the regolith (boundary shown by the red dashed line) (a); scale bar size: 10 cm. Mid slope pits (S- and N-facing) are affected by mass movement downslope, leading to an accumulation of angular fragments in the soil columns (b). (For interpretation of the references to color in this figure legend, the reader is referred to the web version of this article.)
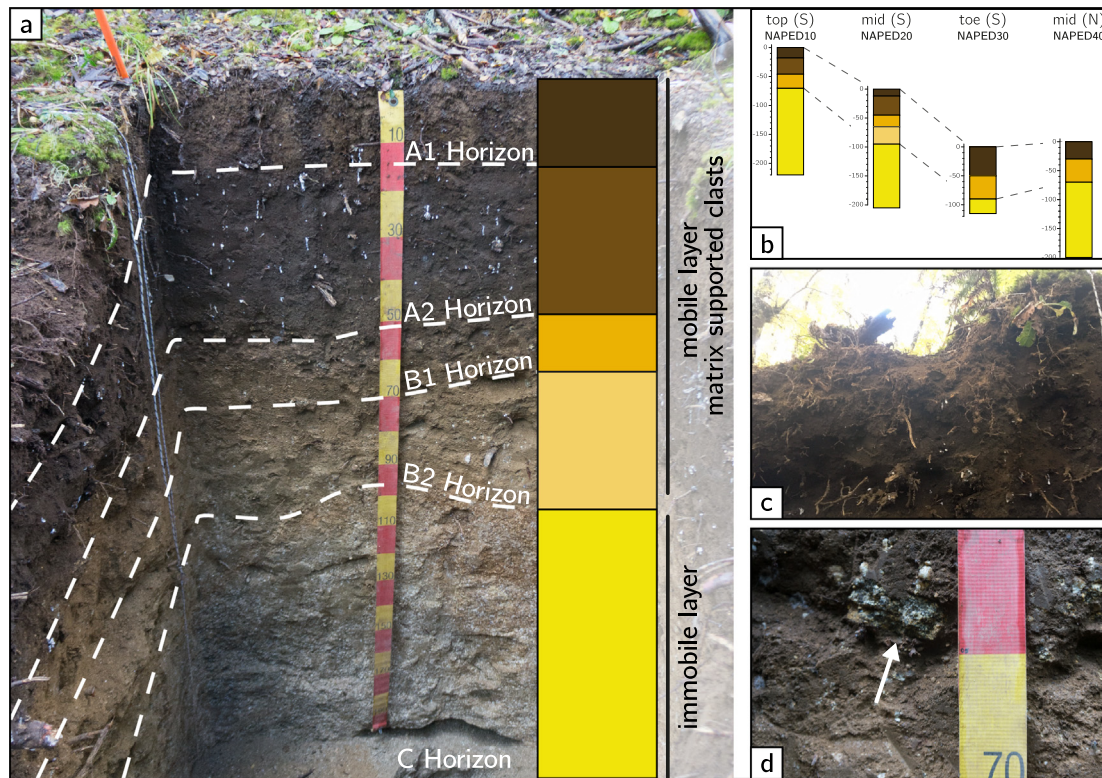
Fig. 6. Photographs of the S-facing mid slope pit (NAPED 20) in Parque Nacional Nahuelbuta (NA) including horizon boundaries (white dashed line), a profile sketch, and a cross section through the S-facing catena and adjacent N-facing pit. Very high organic matter content, characterize the upper horizons of the four pits (a). Fragments are absent in the regoliths' A-Horizon; they occur in the B-Horizon in the form of weathered granodiorite (b). Rare fragments of mafic composition are also found.

filled with fine-grained material of unknown composition or with visible calcite and gypsum crystals (Fig. 3d). At the base of the regolith profiles, the width of the joints decreases; the joints pinch out to the bottom. Unweathered parent material was not observed. Dead root material has been found in the profiles only rarely.

The area belongs to the vegetation formation "Mediterranean coastal desert scrub of *Euphorbia lactiflua* and *Eulychnia saint-pieana*" (Luebert and Pliscoff, 2006). The vegetation cover is very low (< 10%) and is represented only by small shrubs, geophytes and annual plants (Armesto et al., 1993), which are present in more abundance in small ravines. On the sampled S-facing slope, a few individuals of *Tetragonia maritima*, *Nolana mollis*, *Perityle* sp. and *Stipa plumosa* can be found. On the N-facing slope, single individuals of *N. mollis* and *Cristaria integerrima* are present. From these species, only *T. maritima*, *N. mollis* and *C. integerrima* maintain their vegetative structures during dry years.

2.2.2. Santa Gracia

In the natural reserve of *Santa Gracia* (SG) the three S-facing regolith profiles are located on a 153-m long slope. The N-facing regolith profile is located at a distance of 160 m from the S-facing mid-slope profile. The elevations of these four profiles range from 628 to 718 m a.s.l. with the two mid-slope profiles at approximately 690 m a.s.l. Slope angle is slightly lower than in Pan de Azúcar and varies between 15 and 25° at the mid-slope regolith profiles (Fig. 4b; Table S1).

The surface of the regolith profiles in Santa Gracia is composed of sub-angular, coarse sand-sized quartz and granodiorite fragments. This brownish A horizon is made of grussified granodioritic, silt to fine sand-sized particles, supporting fragments of up to 2 mm in diameter. Roots are abundant in this horizon and reach diameters of up to 1 cm (Fig. 4). This horizon is underlain by a brownish white-spotted transitional (B) horizon. Within this horizon, the proportion of fragments increases with their size, resulting in a fine-grained matrix that is supported by coarse

fragments at the horizon's base. Fine roots pervade this horizon. The extent of the soil horizon (comprised of A and B horizon) increases from the top- to toe-slope regolith profiles of the S-facing slope from 30 to 55 cm (Table S1). The depth of the soil horizon in the regolith profile on the N-facing slope (SGPED70) is thinner (35 cm) and its brownish color less dominant.

The orange-brownish saprolite is dominated by greenish-black weathered biotite and hornblende and reddish feldspars, respectively. Fragments are up to 1 cm in size and are surrounded by fine-grained material and fine roots. Joint spacing in the weathered granodiorite is approximately 30 cm. Roots (average diameter of 1 mm) penetrate the fractures and weather the adjacent rock face (Fig. 4d). In contrast to the S-facing regolith profiles, the weathered bedrock in the N-facing regolith profile exhibits a white and gray mottled pattern at depth, with only a few orange spots visible.

The vegetation belongs to the "Interior Mediterranean desert scrub of *Heliotropium stenophyllum* and *Flourensia thurifera*" formation (Luebert and Pliscoff, 2006). The original vegetation has been highly disturbed and the current shrubby vegetation is influenced by livestock grazing (mostly goats; Bahre, 1979). For these reasons, combined with the semi-arid climate, vegetation cover is low, especially in the herbaceous layer. The shrub layer is sparse (~ 30–40% cover) and is dominated by *Proustia cuneifolia* and *Senna cumingii* on the sampled S-facing slope, and by *Cordia decandra* and *Adesmia* sp. on the N-facing slope. On the latter slope, the cactus *Cumulopuntia sphaerica* is very abundant and the columnar cactus *Eulychnia acida* is present with individuals of > 2 m height (i.e. cardonal vegetation community; Bahre, 1979). In the area, some individuals of the shrubs *Balbisia peduncularis*, *Baccharis paniculata* and *Bulnesia chilensis* also occur.

2.2.3. La Campana

The regolith profiles in *La Campana national park* (*LC*) are located on

a S-facing slope of 152 m length where the S-facing and the N-facing mid-slope regolith profiles are separated by 173 m. The elevations of the four profiles range from 706 to 750 m a.s.l. with the two mid-slope profiles being at 730 and 734 m a.s.l., respectively. The mean slope angle at the mid-slope profiles is around 18° (Fig. 5b; Table S1).

The regolith at this site is covered by an O horizon of a few centimeters thickness, composed of litter and tree-debris mixed with granitic gruss of sand size. The dark-brown A horizon on the S-facing *catena* has a thickness of up to 40 cm. In contrast, the N-facing regolith profile's A horizon is of grayish-brown color and measures only 12 cm. It is composed of fine-sand to silt-sized particles, hosting some granodioritic fragments of up to 3 mm in diameter and is highly permeated by roots of various sizes. The base of the soil horizon is characterized by a brown to orange-brown transitional (B) horizon. As the matrix is coarsening downwards, the number of fragments increases and the horizon shifts from a matrix- to a clast-supported one. The final transition from soil to saprolite occurs at a depth of 60 cm within 3 to 5 cm. At the N-facing slope, this transition occurs at a shallower depth.

The saprolite develops from (at least) two distinct granodiorite types: a coarse-grained and a fine-grained one (Fig. 5c). In both cases, the granodiorite fabric is still visible and the mineral composition (plagioclase ≫ quartz ≫ K-feldspar & biotite) is similar. Throughout the saprolite, fine roots are common and are most abundant within fractures.

The vegetation of La Campana belongs to the "Coastal Mediterranean sclerophyllous forest of *Lithraea caustica* and *Cryptocarya alba*" formation (Luebert and Pliscoff, 2006) and includes examples of all the major biotic communities of sclerophyllous forest of central Chile (Gajardo, 1994; Rundel and Weisser, 1975). Vegetation cover is high, with almost 100% ground cover. The forest canopy is dominated by the evergreen sclerophyllous trees *L. caustica*, *C. alba*, *Quillaja saponaria*, and in lower abundance *Kageneckia oblonga*. The medium shrub layer is dense and dominated by *Colliguaja odorifera*, *Aristeguietia salvia* and *Retanilla trinervia*, and in less abundance *Podanthus mitiqui*. The herbaceous layer presents a high cover and diversity and is especially rich in annual species. The most abundant species are *Geranium robertianum*, *Stellaria media* and the fern *Adiantum chilense*. Along the S-facing *catena*, the trees *L. caustica* and *C. odorifera* are the most abundant and dominant species. In less abundance, *P. mitiqui* and *A. salvia* are found in the shrub layer, while the herbaceous layer is dominated by *Alstroemeria* sp., *G. robertianum*, *S. media*, *Solenomelus pedunculatus* and *A. chilense*. Near the N-facing slope profile, high vegetation is less abundant and less rich in species. The canopy is strongly dominated by *L. caustica*, accompanied by some individuals of *Jubaea chilensis*. The most abundant shrub is *R. trinervia*, followed by *A. salvia* and *C. odorifera*. *Poaceae* spp. and *Sonchus oleraceus* dominate the herbaceous layer, where climbing species like *Tropaeolum* sp. and *Dioscorea* sp. also occur.

2.2.4. Nahuelbuta

The regolith profiles in the *Nahuelbuta national park* (*NA*) are located on a 136-m long S-facing slope where the S-facing and the N-facing mid-slope regolith profiles are separated by 145 m. The elevations of these four profiles range from 1219 to 1248 m a.s.l., being the highest among the four study sites. Slope angles of around 14° at the mid-slope profiles are the smallest of the study area (Fig. 6b; Table S1).

The regolith at Nahuelbuta is covered by a 2 to 5 cm thick O horizon, almost entirely composed of roots, leaves, and moss. The A horizon is characterized by a large number of roots (various sizes, up to 3 cm in diameter; Fig. 6) and a brown to black color. This horizon is mainly composed of silt-sized particles, forming nodular soil aggregates, giving this layer a granular texture. In the upper part of the A horizon, up to 1 mm large quartz grains are embedded and at the base, larger granodioritic fragments occur. The transitional (B) horizon increases in thickness from the top to the toe slope regolith profile on the S-facing *catena*. Its matrix is made of fine-sand sized particles, hosting sub-angular granodioritic fragments. As depth increases, fragment

abundance and size is increasing and the horizons' color is lighter. Unlike in the upper two S-facing regolith profiles, where the transition from soil to saprolite is gradual, the S-facing toe slope and the N-facing mid-slope profile are characterized by a thin soil-saprolite transition zone. At this transition, highly weathered mafic rock (NAPED30) and granodioritic core stones (NAPED40) appear, respectively.

The saprolite is coarse-grained and disaggregates readily. Its color varies from dark gray to whitish. The dark color is attributed to weathered bedrock of mafic composition and the whitish color to weathered rock with an increased plagioclase abundance. Some reddish intercalations within the saprolite follow fluid pathways along formerly open fractures and pathways once occupied by roots.

The dominant vegetation belongs to the "Coastal temperate forest of *Araucaria araucana*" formation (Luebert and Pliscoff, 2006). Here also, vegetation cover is 100%. The general area also supports tall evergreen mixed forest dominated by the broadleaved *Nothofagus dombeyi* and the iconic conifer *A. araucana*, but around the soil pits the forest is more open and dominated by the lower-stature deciduous trees *Nothofagus obliqua* and *Nothofagus antarctica*, together with the tall *A. araucana*. The dominant shrub species is *Gaultheria mucronata*, but other species like *Azara microphylla*, *Baccharis* sp., *Ribes magellanicum* and *Berberis montana* are also present. At the herbaceous level, *Stipa* sp. and *Mutisia decurrens* are very abundant. However, herbaceous diversity is very high and is also represented by e.g. *Chusquea culeou*, *Bromus* sp., *Viola maculata* and *Adenocaulon chilense*. Around the regolith profile on the N-facing slope, *N. obliqua* and *N. antarctica* are the most abundant species in the canopy and the understory is dominated by *G. mucronata* and *Stipa* sp. Along the catena on the S-facing slope, the canopy is less dense and *A. araucana* is the most abundant species, followed by *N. antarctica*, while in the understory *C. culeou* is very common. Lichens of the genus *Usnea* abundantly cover most of the tree trunks and branches.

3. Material and analytical methods

3.1. Sampling

Regolith samples were collected from bottom to top (if applicable) in a continuous sequence of depth increments, amounting to a thickness of 5 cm (uppermost two samples), 10 cm (3rd sample from top), and 20 cm (4th sample from top and below), respectively. About 1 kg of material was taken per sample. In addition, saprolite samples (50 ml) were taken under sterile conditions for DNA-based analyses of microbial abundances. These latter samples were stored and transported under frozen conditions to Germany.

Underlying unweathered bedrock has not been reached in the regolith profiles of this study and the depth to bedrock remains unknown. However, a set of 20 bedrock samples (4 in Pan de Azúcar, 8 in Santa Gracia, 5 in La Campana and 3 in Nahuelbuta, respectively) was thus obtained from nearby outcrops.

All sample metadata are already available on a public server using unique sample identifiers in form of the new "International Geo Sample Number" (IGSN).

3.2. Bedrock and regolith geochemistry

Major and trace element concentration of bedrock and regolith samples were determined using the PANalytical AXIOS advanced X-Ray Fluorescence spectrometer at the GFZ German Research Centre for Geosciences, Section "Inorganic and Isotope Geochemistry". The device is equipped with a Rh anode X-ray tube, which was operated at an excitation voltage of 25 to 60 kV and currents between 60 and 160 mA. Measuring times for major elements varied between 10 and 20 s, for trace elements it was set to 40 s.

Prior to measurement, each sample was milled in an agate mortar and sieved through a 62 μm gauze sieve. Powdered samples were dried at 105 °C for 24 h before glass bead preparation. Glass beads were made

with 1 g of sample material, 6 g of dilithiumtetraborate, and up to 1 g of ammonium nitrate, brought to complete fusion in a heating system in six steps of up to 8-minute intervals. The intervals were adjusted depending on the concentration of organic compounds. The loss on ignition for each sample was determined by weighing the glass beads and the platinum crucibles used for glass bead preparation before and after fusion.

XRF data of regolith samples have been recalculated to a volatile free basis using.

$$[X]_{recalc} = \frac{[X_{measured}]}{SUM_{measured} - (LOI_{measured} - \overline{LOI_{bedrock}})}, \tag{1}$$

where [X]$_{recalc}$ and [X$_{measured}$] refers to the recalculated and measured concentration of an element, SUM$_{measured}$ to the sum of all elements analyzed, and LOI$_{measured}$ to the samples' loss on ignition, respectively. LOI$_{bedrock}$ is the average loss on ignition of associated bedrock samples.

Pedogenic oxides of Iron (Fe), Aluminum (Al), Manganese (Mn), and Silicon (Si) were determined at University Bern with the dithionite-citrate method as described by Mehra and Jackson (1958). Active oxides of the same elements were examined as ammonium-oxalate extractable compounds (Schwertmann, 1964; modified after Tamm, 1922). Oxides associated with soil organic matter (SOM) were extracted with a 0.1 M pyrophosphate reagent (Na$_2$P$_2$O$_7 \times$ 10 H$_2$O) at pH 10. Elements have been analyzed on an ICP-MS (7700x Agilent Technologies).

Mineral assemblages and approximate mineral abundances in representative bedrock samples were estimated at GFZ Potsdam using thin section microscopy and standard point counting techniques.

3.3. Cosmogenic ^{10}Be in quartz

For determination of the in situ-produced ^{10}Be concentration in quartz, the saprolite samples were washed, dried, and sieved to a fraction of 0.25 to 2.0 mm at the University of Tübingen, Department of Geosciences, Germany. The 1.0 to 2.0 mm fraction was crushed to 0.25 to 1.0 mm. After magnetic separation and treatment with HCl, the sample material was leached with HF/HNO$_3$. The remaining non-quartz minerals were dissolved and meteoric ^{10}Be was removed from quartz grains by HF etching. A total of 15 to 35 g of cleaned quartz was spiked with ~ 0.3 mg ^{9}Be and dissolved with concentrated HF. Beryllium was separated from other elements with column chromatography and precipitation techniques after von Blanckenburg et al. (1996). After oxidation BeO was mixed with Nb powder for measurement of ^{10}Be/^{9}Be ratios at the accelerator mass spectrometer (AMS) facility in Cologne. Uncertainty on measured ratios is reported as 1σ. Calculated sample concentrations were corrected for a combined mass spectrometry and chemistry blank of 3.4 × 10^4 atoms.

3.4. DNA extraction and quantification of 16S rRNA gene copies

Total genomic DNA was extracted at GFZ Potsdam from saprolite samples which were collected under sterile conditions. The PowerSoil® DNA Isolation Kit was used for soils from La Campana, Santa Gracia, and Nahuelbuta with a maximum sample amount of 0.25 g each. Samples from Pan de Azúcar were treated with the PowerMax® Soil DNA Isolation Kit (both from MoBio Laboratories, CA, USA). Before processing, saprolite samples from Pan de Azúcar and Santa Gracia were crushed by hand. Following this, DNA was extracted in triplicates following the manufacturer's protocol with one exception; DNA elution was done with PCR-grade water. Final concentrations were measured with a NanoPhotometer® (P360, Implen GmbH, Germany). Purity was controlled by the optical density values of OD$_{260}$/OD$_{280}$ and OD$_{260}$/OD$_{230}$.

Gene copy numbers of universal bacteria and universal archaea were determined by quantitative polymerase chain reaction (qPCR). 16S rRNA genes were amplified by using the bacterial primer pair Eub341F (5′–CCT ACG GGA GGC AGC AG–3′) and Eub534R (5′–ATT

ACC GCG GCT GCT GG–3′) (Muyzer et al., 1993), and the archaeal primer pair 340F (5′–CCC TAC GGG GYG CAS CAG–3′) and 1000R (5′–GGC CAT GCA CYW CYT CTC–3′) (Gantner et al., 2011). The qPCR assay was carried out in a total reaction volume of 20 µl using the KAPA SYBR® FAST qPCR Kit Master Mix (2X) Universal (Kapa Biosystems, Sigma-Aldrich, Germany) in accordance with the manufacturer's recommendations. Quantification was performed in the CFX96 Connect™ Real-Time System (Bio-Rad Laboratories, CA, USA) with the following cycling program for bacterial 16S rRNA genes (and archaeal 16S rRNA genes): initial denaturation at 95 °C for 3 min, followed by 40 (45) cycles of denaturation at 95 °C for 3 s, annealing at 60 °C (57 °C) for 20 s, elongation at 72 °C for 30 s. Fluorescence was measured at 80 °C. The melting curve was recorded by rising temperature from 65 to 95 °C. Due to preliminary experiments, DNA extracts were used in 1:10 for archaea and 1:100 dilutions for bacteria to avoid putative inhibitions of co-extracted substrates. Every qPCR run included blanks, calibration standards in triplicates and saprolite samples in quadruplicates. The reaction efficiency ranged between 92.0 and 98.6%. Data analysis was carried out using the CFX Manager™ Software (Bio-Rad Laboratories, CA, USA).

4. Calculation of weathering indicators and denudation rates

To quantify the element fluxes as well as the weathering intensities that emerge when the bedrocks' elements are solubilized in percolating fluids and new elements are introduced from the atmosphere, various indices and coefficients have been developed. The common denominator of all these approaches is the identification of an element considered to be immobile during weathering. Furthermore, cosmogenic nuclide concentration can be converted into rates of mass removal. In the following, we outline these quantification approaches.

4.1. Chemical index of alteration (CIA), chemical depletion fraction (CDF), mass transfer coefficient (τ), and volumetric strain (ε)

To assess the relative degree of chemical weathering, we used the CIA (Eq. (2)) developed by Nesbitt and Young (1982). In this approach, aluminum is assumed to be an immobile element and the degree of weathering is traced by comparing the aluminum content of a sample with this of the readily soluble cations calcium, sodium and potassium in silicate minerals.

$$CIA = \frac{Al_2O_3}{Al_2O_3 + CaO + Na_2O + K_2O} \times 100. \tag{2}$$

The CIA in unweathered granitoid rock has values of 45 to 55. The degree of weathering has to be evaluated from the CIA in weathered material relative to its respective unweathered precursor. As weathering proceeds the CIA evolves to a maximum value of 100 (Nesbitt and Young, 1982).

To calculate the relative mass loss caused by chemical weathering of the parent rock we used the chemical depletion fraction (CDF; Riebe et al., 2003):

$$CDF = 1 - \frac{[X_i]_{parent}}{[X_i]_{weathered}} CDF = 1 - \frac{[X_i]_{parent}}{[X_i]_{weathered}}, \tag{3}$$

where [X$_i$]$_{weathered}$ and [X$_i$]$_{parent}$ represent the concentration of the immobile element X$_i$ in weathered regolith and unweathered parent bedrock, respectively. If no element loss has occurred during the transition from parent rock to regolith, the CDF is zero. If weathering has proceeded to completion (i.e. only quartz, clay minerals, and secondary oxides remain), the CDF attains a maximum value of ca. 0.5 in granitic rock.

To estimate the relative loss of individual elements (X), we used the mass transfer coefficient τ (tau; Anderson et al., 2002; Brimhall and Dietrich, 1987). It is important to note that the ratio of X in weathered material to X in unweathered parent rock depends on both the loss of X

and the loss of other elements besides X. To take the loss of other elements into account, the calculation of τ involves concentrations of an immobile element X_i in parent material relative to weathered material:

$$\tau_X = \frac{[X]_{weathered}}{[X]_{parent}} \times \frac{[X_i]_{parent}}{[X_i]_{weathered}} - 1. \tag{4}$$

If τ = 0 no loss of X has occurred compared relative to the parent material. τ < 0 denotes relative elemental loss, τ > 0 denotes gain, respectively.

The conversion of primary minerals into secondary phases and solutes is usually accompanied by a change in density ρ and volume V. A measure of this change and an estimate of deformation is the volumetric strain ε (Brimhall and Dietrich, 1987):

$$\varepsilon = \frac{\rho_{parent}}{\rho_{weathered}} \times \frac{[X_i]_{parent}}{[X_i]_{weathered}} - 1. \frac{[X_i]_{parent}}{[X_i]_{weathered}} \tag{5}$$

Positive values of ε indicate dilation, negative ones collapse of a profile. Values near zero are evidence of isovolumetric weathering.

4.2. Denudation rates based on cosmogenic nuclides and immobile elements

At each primary study site, the total denudation rate D (in $t\,km^{-2}\,yr^{-1}$) was determined for the mid-slope regolith profile of the S-facing and N-facing *catena* (AZPED50 & 21, SGPED40 & 70, LCPED20 & 40, and NAPED20 & 40; Table S6). To ensure that the calculated D reflects that of the regolith profiles and is not influenced by mixing of the surface layer with material from above (e.g. Heimsath et al., 1997), mobile material from the soil layer was avoided. Thus, we determined the in situ-produced ^{10}Be concentrations in quartz from material sampled from the top of the physically immobile saprolite just below the mobile soil layer (see Schaller et al., 2018). D measures the total mass loss within the adsorption depth of cosmic rays (ca. 1 m; e.g. Dixon et al., 2009; Riebe and Granger, 2013; Riebe et al., 2001), which entails chemical loss (weathering, W) and physical loss (erosion, E):

$$D = E + W \tag{6}$$

If mass loss by weathering occurs beneath the cosmic ray adsorption depth, as it is likely in the saprolite that is weathered at great depth in the Chilean Coastal Cordillera (Vázquez et al., 2016), then the ^{10}Be concentration does not account for this loss and D is a minimum estimate (Riebe and Granger, 2013). Nucleonic, stopped muonic, and fast muonic production rates P at sea level and high latitude (SLHL) used for

denudation rate calculation are $3.92\,atoms\,g^{-1}\,yr^{-1}$ (Borchers et al., 2016), $0.012\,atoms\,g^{-1}\,yr^{-1}$, and $0.039\,atoms\,g^{-1}\,yr^{-1}$, respectively (Braucher et al., 2011). SLHL production rates were scaled to sample altitude and latitude with the online tool of Marrero et al. (2016) using the scaling procedure based on Lifton et al. (2014). Shielding factors for topography and slope are 1.0. No shielding by snow has been taken into account. However, in order to correct for the influence of increasing vegetation cover on the production rate, shielding by vegetation of 2.3% for acadian/boreal forest and 7.3% for rain forest have been applied in La Campana and Nahuelbuta, respectively (Plug et al., 2007). Shielding factors due to sample overburden (depth and soil density) were calculated for nucleonic, stopped, and fast muonic production rates. The adsorption lengths used were 157, 1500, and $4320\,g\,cm^{-2}$, respectively (Braucher et al., 2011). Denudation rates D [$t\,km^{-2}\,yr^{-1}$] were calculated based on the blank-corrected nuclide concentrations [$atoms\,g^{-1}$], the ^{10}Be decay constant $\lambda = 4.99 \times 10^{-7}\,yr^{-1}$ (Chmeleff et al., 2010; Korschinek et al., 2010), and the respective production rates P [$atoms\,g^{-1}\,yr^{-1}$] at sample depths and adsorption lengths Λ [$g\,cm^{-2}$] for each production mechanism using Eq. (7):

$$D = \left(\frac{P}{[^{10}Be]} - \lambda\right)\Lambda \tag{7}$$

The weathering rate can be calculated from D by using the CDF, which is a measure of the fraction of the total denudation that is accounted for by chemical weathering or also the ratio of chemical weathering to total denudation W/D. W is given by:

$$W = D \cdot CDF. \tag{8}$$

We determined W with the CDF averaged over all soil samples, thus calculating a maximum chemical loss over the entire regolith profile.

5. Results

5.1. Chemical and mineralogical bedrock composition and classification

Major and selected trace element concentrations and density of local bedrock for each of the study sites are listed in Table S2. The bedrock in Pan de Azúcar and La Campana is characterized by $SiO_2 > 71$ wt% and a high Na_2O and K_2O content (~7 wt%; Fig. 7a). Apart from Mg, Ca, and Ba, major and trace elements show uniform concentrations (i.e. standard deviations below 15%). In contrast, bedrock samples from Santa Gracia and Nahuelbuta show extensive compositional
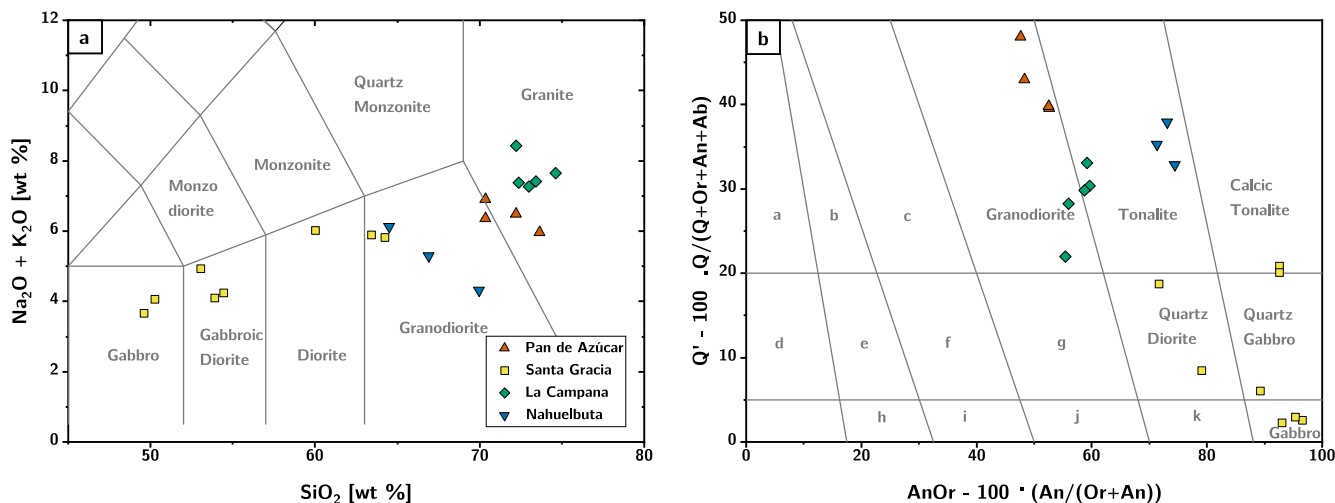
Fig. 7. Classification diagrams for siliceous igneous and volcanic rocks. (a) Total alkali versus silica diagram introduced by Le Bas et al. (1986). (b) Q-AnOr diagram of Streckeisen and LeMaitre (1979), where the mineral modes were determined from XRF analyses by the CIPW norm calculation. Field association as follows: a - Alkali-feldspar granite; b - Syenogranite; c - Monzogranite; d - Alkali-feldspar Quartz Syenite; e - Quartz Syenite; f - Quartz Monzonite; g - Quartz Monzodiorite; h - Syenite; i - Monzonite; j - Monzogabbro; k – Diorite.

heterogeneities. In Santa Gracia and Nahuelbuta, the standard deviation of the major and trace element concentrations is 33 and 50%, respectively. At Santa Gracia, the SiO_2 concentration is by far the lowest (50 wt% < SiO_2 < 64 wt%) whereas the MgO concentration is the highest (0.91 wt% < MgO < 5 wt%) of all analyzed bedrock samples. The major element bedrock composition at Nahuelbuta is similar to that of Santa Gracia with the exception of SiO_2 concentrations that are 65–70 wt%.

Modal mineral abundances based on CIPW norm calculation (Johannsen, 1937) of average bedrock composition for each study site are given in Table S3. With the exception of Santa Gracia, bedrock composition includes quartz (≥ 35 vol%) and feldspar-rich (Pl ≥ 35 vol %; Kfs ≥ 17 vol%) granitoid rocks. According to the two classification

schemes of igneous and volcanic rocks introduced by Le Bas et al. (1986; Fig. 7a) and Streckeisen and LeMaitre (1979; Fig. 7b), the bedrock samples from Pan de Azúcar, La Campana, and Nahuelbuta are granites, granodiorites, and tonalites, respectively. Santa Gracia bedrock yield CIPW-based mineral modes for plagioclase- (An + Ab) of 67 vol%, pyroxenes (14 vol%), quartz (9 vol%), and K-feldspar (5 vol%) rock. Both schemes classify these rocks as gabbros and diorites – igneous rocks with a low quartz content.

5.2. Regolith chemistry and weathering patterns

Major element concentrations of the four regolith profiles at each site are shown in Table S4 and Fig. 8. The principle differences in the
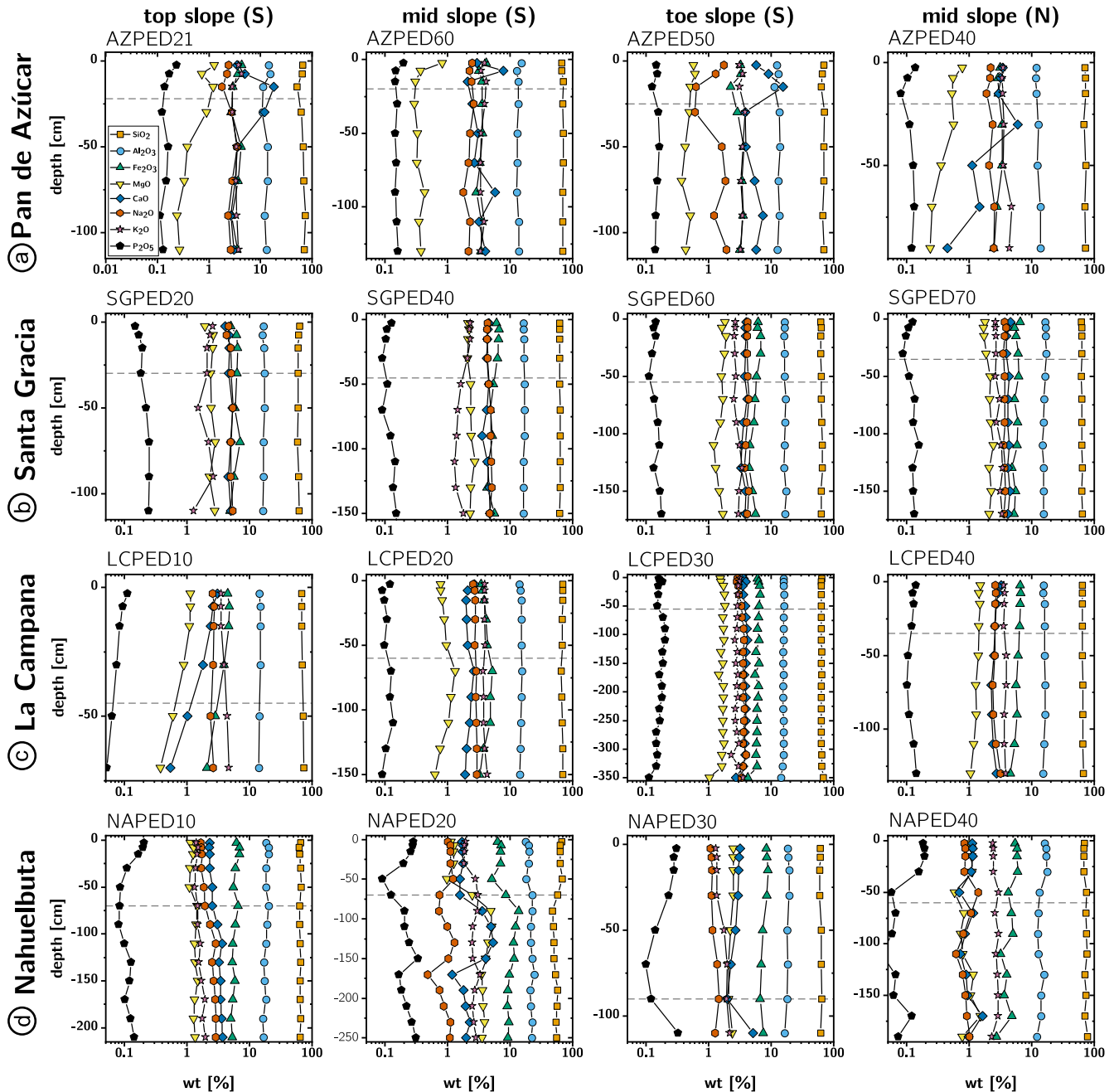
Fig. 8. Depth-dependent major element composition (corrected for LOI following Eq. (1)) of the four primary EarthShape study sites (regolith profile names indicated above). Differences between sites are attributed to large-scale bedrock variations and differences within the single *catena* to small-scale lateral and vertical bedrock heterogeneities. Vertical variations within a profile (i.e. LCPED30, NAPED20, NAPED40) reflect a change in substrate. Dashed lines indicate the soil – saprolite boundary.
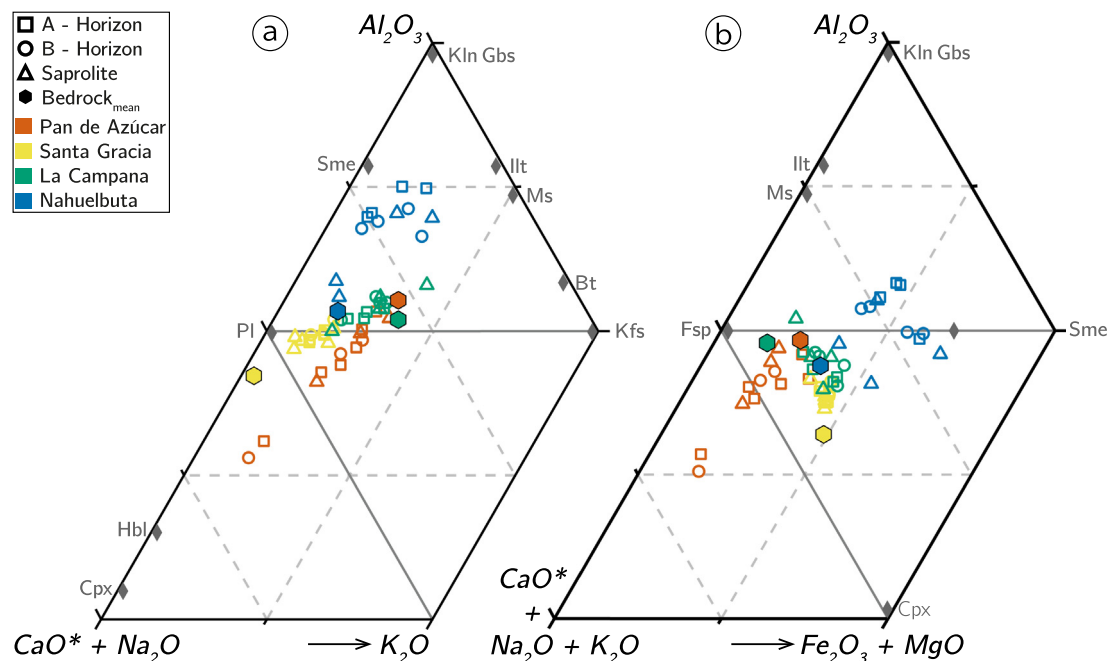
Fig. 9. Weathering trends for regolith profiles in Pan de Azúcar (red), Santa Gracia (yellow), La Campana (green), and Nahuelbuta (blue) in the ternary space of A-CN-K (a) and A-CNK-FM (b) as introduced by Nesbitt and Young (1982) (molar proportions). Note that (a) corresponds to the CIA which is 100 at pure Al_2O_3, and 50 at connecting line between Pl and Kfs. The gray diamonds represent idealized mineral compositions: Bt - biotite; Cpx - clinopyroxene; Fsp - feldspar; Gbs - gibbsite; Hbl - hornblende; Ilt -illite; Kfs - K-feldspar; Kln - kaolinite; Ms. - muscovite; Pl - plagioclase; Sme – smectite. (For interpretation of the references to color in this figure legend, the reader is referred to the web version of this article.)

overall compositions between the sites reflect the differences in bedrock composition. The compositional heterogeneity is small in Pan de Azúcar, Santa Gracia and La Campana within the saprolite. Only at Nahuelbuta the saprolite shows a high level of compositional heterogeneity between and within profiles, which is due to initial bedrock heterogeneity. Importantly, no gradients towards the base of the profiles are observed, implying that the weathering front has not been reached in any of these profiles. A and B horizon samples have a higher degree of heterogeneity, with some showing an increase in P and Ca concentrations.

The compositional features translate into the following patterns of weathering intensity (CIA, Fig. 9). CIA of the EarthShape bedrock samples lie within the typical range of granitoid rocks (44–55; Nesbitt and Young, 1982; Table S5). The CIA at Pan de Azúcar ranges from a bedrock average value of 55 ± 1 to a value as low as 32 in soil and saprolite (Table S5). This trend is opposite to that expected from weathering and is presumably due to atmospheric additions (see also Bernhard et al., 2018). The CIA at Santa Gracia ranges from a bedrock value of 43 ± 4 to 52 in regolith, which is due to the reaction of plagioclase to clay (Fig. 9a; Table S5). At La Campana the bedrock CIA value is 52 ± 1. The range of CIA of regolith samples between 50 and 58 is similar and indicates a low degree of weathering (Table S5). The bedrock CIA at Nahuelbuta is 54 ± 1, regolith samples show progressively increasing CIA values (Table S5) from 56 in saprolite to 75 in the A horizon. Thus, the degree of chemical weathering in the study area is generally relatively low, except for Nahuelbuta, and increases from Pan de Azúcar to Nahuelbuta.

5.2.1. Assessing Zr and Ti immobility in the study area

Zr, Ti, and Nb are commonly assumed to be least mobile during weathering (Chadwick et al., 1990; White et al., 1998) and are thus used in estimates of mass loss in the dissolved form during weathering (Eqs. (3) & (4)). We first evaluated the suitability of these elements on a case to case basis, as their abundance can be biased from rock values by heterogeneity, loss, or external inputs. In Fig. 10 we perform this

evaluation for Zr and Ti. A line (i.e. weathering enrichment line, including uncertainty envelopes representing bedrock heterogeneity) was constructed from the initial Ti/Zr ratios of bedrock samples. The line describes the expected relationship between these elements' concentration in regolith if they were entirely immobile during chemical weathering, and if a change in their concentration is solely due to weathering (i.e. no external input, no differential mobility), such that their concentrations increase in proportion to each other by loss of other elements (Hewawasam et al., 2013).

Only Zr and Ti concentrations in regolith samples in Pan de Azúcar and La Campana roughly plot on the weathering enrichment line (Fig. 10a, c). In La Campana, exceptions are restricted to LCPED30 (Fig. 10c) and are most likely caused by compositional heterogeneities of the regoliths' parent material (Table S2). In Santa Gracia, regolith samples plot exclusively below the weathering enrichment line (Fig. 10b). Ti loss cannot be excluded, given the higher solubility of Ti-bearing minerals (i.e. biotite, titanite) when compared to zircon. In Nahuelbuta, most soil samples plot along the weathering enrichment line, but saprolite samples scatter widely (Fig. 10d). The high concentration of Ti in the saprolite and B horizon of samples from NAPED20 and NAPED40 can only be explained by heterogeneity in the substrate. Based on the possibility that Ti is mobile in some samples and the fact that Zr is used as a reference element in the majority of weathering and soil production studies worldwide (e.g. Green et al., 2006; Hewawasam et al., 2013; Riebe and Granger, 2013; Riebe et al., 2001; Uhlig et al., 2017), we will use Zr as immobile reference element in our study.

5.2.2. Chemical depletion fraction (CDF)

Whereas the CIA presented above describes relative weathering trends, the CDF quantifies elemental loss. The CDF has been calculated using the study sites' average bedrock Zr concentration. The median CDF of the entire sampled regolith is between 0.2 and 0.5 for Nahuelbuta, La Campana, and Santa Gracia. At these sites, the CDF in the A and B horizon is also higher than that in the saprolite (Fig. 11).
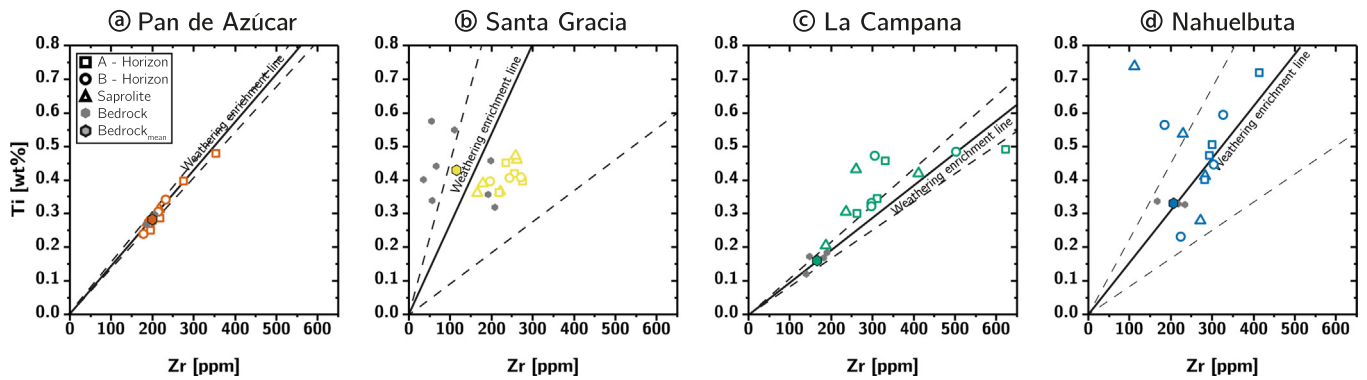
Fig. 10. Ti and Zr concentration measured in soil, saprolite, and bedrock at the four primary EarthShape study sites. Solid lines (with error envelope, dashed) indicate the weathering enrichment line for bedrock composition, constructed from initial element ratios from bedrock samples and their uncertainty, as quantified by the Ti and Zr concentration of multiple bedrock samples.

This increase in the intensity of weathering between saprolite and soil is most pronounced in the S-facing mid-slope profile at Santa Gracia (weathering intensity increase by 28%) and in the top-slope pit at La Campana (weathering intensity increase by up to 35%; Table S5). Only in Pan de Azúcar the degree of weathering as quantified by the CDF is very low: at this site, the saprolite CDF is zero within uncertainty and only the thin A horizon shows some loss with a median CDF of 0.1. The B horizon shows enrichment (CDF < 0), which is due to atmospheric input and the formation of gypsum and calcite precipitates in this horizon. Differences in the degree of weathering between N- and S-facing regolith profiles are either not resolvable or, as in Nahuelbuta, caused by substrate heterogeneities within the profile. However, all CDF values are subject to high uncertainties, as shown by the standard deviation of the pooled samples at each site (Fig. 11). These uncertainties stem from the chemical heterogeneity in the bedrock (Figs. 7 & 10; Table S2) and heterogeneities within the regolith profiles (Fig. 10; Table S4). This limits the attainable resolution in CDF to ± 0.04 at Pan de Azúcar, ± 0.6 at Santa Gracia, and ± 0.1 for Nahuelbuta and La Campana (Table S5). Due to the high uncertainty of the CDF in Santa Gracia, we cannot exclude that the degree of weathering is actually lower than estimated at this site. The large variation in the Zr concentration within the regolith profiles in Nahuelbuta, especially in NAPED20 (Table S4), account for the high variability in CDF values in this study site.

5.2.3. Elemental mass transfer coefficients (τ)

Elemental mass transfer coefficients (τ) have been calculated using the Zr concentration of each regolith profile's lowermost sample as reference since the geochemical heterogeneity of bedrock (Table S2) does not allow the identification of a representative Zr concentration from

rock samples. We thus evaluate vertical structure in elemental loss or gain relative to the base of the regolith profiles, rather than relative to bedrock. For Fig. 12, we averaged τ values for A, B and saprolite horizons within each site (Table S5) to resolve statistically significant patterns for each site.

The regolith at Pan de Azúcar shows almost no losses, but an enrichment (i.e. $\tau > 0$) of Ca and Mg with decreasing depth. At Santa Gracia, averaged τ values for major elements and P in the saprolite indicate neither loss nor gain (i.e. $\tau = 0$; Fig. 12b). These elements are slightly depleted in A and B horizons. In La Campana, only Na and Si are lost in significant proportions from the saprolite (Fig. 12c; Table S5). These elements are progressively depleted with decreasing depth. P and K are depleted in the A and B horizon relative to the saprolite. Significant differences are apparent in the depletion of Ca, Mg, Fe, and Mn between the N- and the S-facing mid slope profile (Table S5). In Nahuelbuta, τ values spread widely around their median values, which we attribute to the large chemical heterogeneity within the parent material (Fig. 12d; Table S4 and S5). In the A and B horizons, τ values indicate moderate (i.e. $\tau_{Ca, K, Mg} \approx -0.25$) to high depletion (i.e. $\tau_{P, Si} \approx -0.60$).

5.2.4. Volumetric strain (ε)

Volumetric strain has been calculated using each study sites' average bedrock density and Zr content (Table S2) along with the regolith samples' bulk density (Bernhard et al., 2018) and Zr content (Table S4). Largest volumetric expansion is seen in saprolite and soil samples from Nahuelbuta, ranging from 0.22 in saprolite to 1.54 in soil (Fig. 13; Table S5). The saprolite in the two sites further north (La Campana and Santa Gracia) experienced neither expansion nor collapse (Fig. 13; Table S5). For Pan de Azúcar, strain values in saprolite have
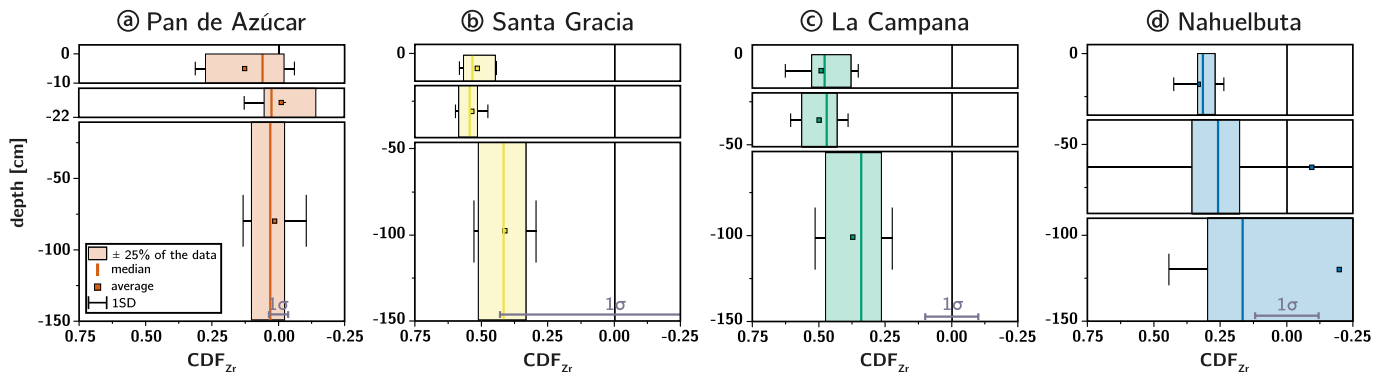
Fig. 11. Chemical Depletion Fraction (CDF) for each study sites' averaged A horizon (top), B horizon (middle) and saprolite (bottom) samples. See legend in panel a for the explanation of the uncertainty bars. The accuracy of the absolute CDF values is limited by the variability in the respective sites' bedrock Zr concentration as indicated by the gray 1σ bar at the graphs' bottom. Note that the Y-axis scale is expanded by a factor of three for the A and B horizon in Pan de Azúcar.
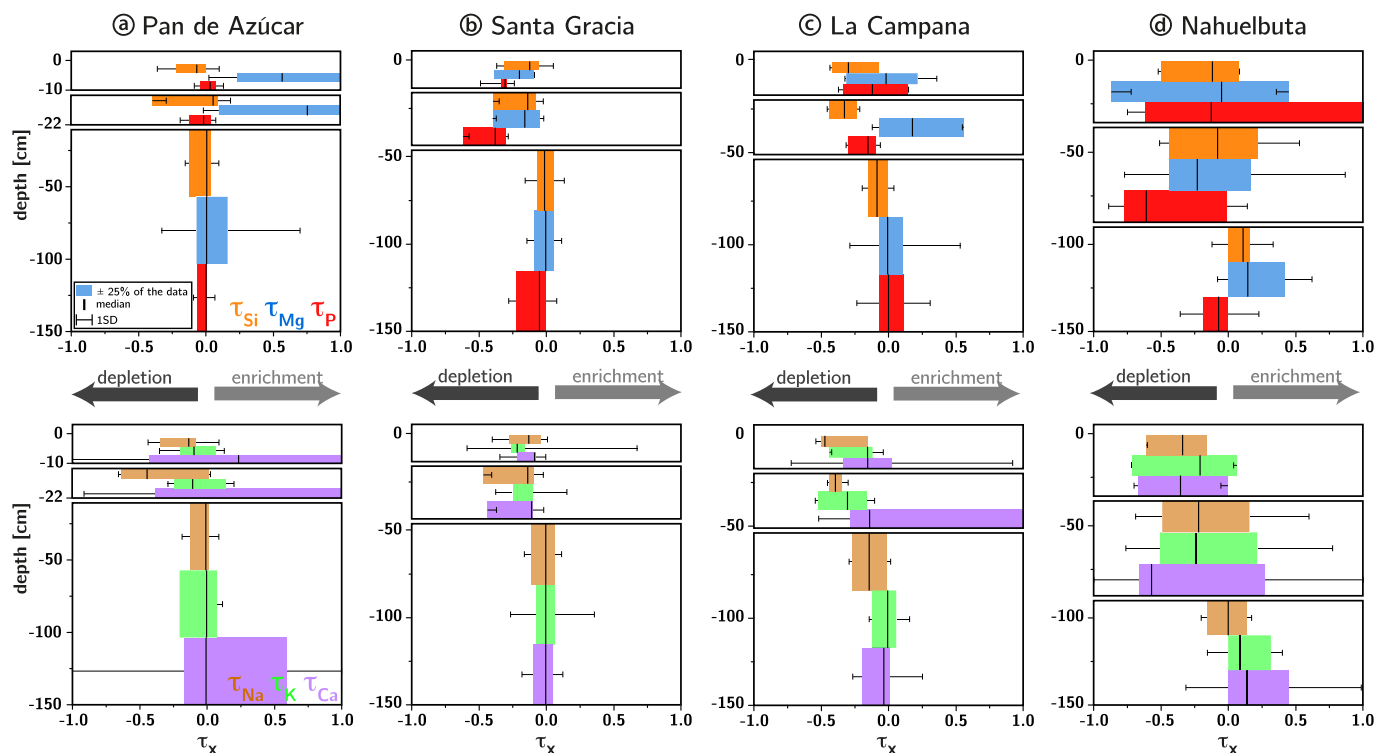
Fig. 12. Elemental mass transfer coefficient (τ, the fractional element loss that was calculated here relative to the sample at the base of the regoliths profile) for each study sites' averaged A horizon (top box), B horizon (middle box), and saprolite (bottom box) samples. The upper graphs show τ values for Si, Mg, and P, whereas the lower graphs show τ values for Na, K, and Ca. Note that the shown τ values are only stacked for visualization reasons and represent τ values averaged over the study sites' specific horizons. Further, the Y-axis scale is expanded by a factor of three for the A and B horizon in Pan de Azúcar.

not been calculated because no measurements of density were available. Whereas the soil horizons in La Campana and Santa Gracia are affected by minor dilation ($\varepsilon \approx 0.25$) and collapse ($\varepsilon \approx -0.25$), respectively, the A- and B-horizons in Pan de Azúcar show a higher volume expansion ($\varepsilon \approx 0.8$; Fig. 13; Table S5).

5.3. Pedogenic oxides

The oxalate-extractable Fe (Fe_o, ferrihydrite and poorly crystalized goethite) and dithionite-extractable Fe (Fe_d, well crystalized goethite, hematite, and lepidocrocite) were normalized to the total samples' Fe concentration determined from XRF analyses (Table S4). The Fe_o/Fe_{tot} ratio in Pan de Azúcar, Santa Gracia, and La Campana ranges from 0.002 to 0.025 with slightly increasing proportions of extractable Fe

towards the A horizon (Fig. 14a–c). Differences between oxalate- and dithionite-extractable Fe are most pronounced in Pan de Azúcar and La Campana. In Nahuelbuta, both the Fe_d/Fe_{tot} and Fe_o/Fe_{tot} ratios increase to values up to 0.24 in the A and B horizons. Pyrophosphate-extractable Fe (Fe_p, organic-bound colloidal Fe) range from 15 to 6870 ppm. The absolute Fe_p concentration substantially increase from La Campana to Nahuelbuta. The northern three study sites' average Fe_p is ~200 ppm.

From the oxalate-extractable Al (Al_o, amorphous Al-Si-OH) and dithionite-extractable Al (Al_d, clay) we have calculated oxalate-extractable (Al_o/Al_{tot}) and dithionite-extractable Al fractions (Al_d/Al_{tot}) that range between 0.1 and 0.2 (Fig. 14). Large differences between the two extracts were observed only in Nahuelbuta and to some extent in Santa Gracia (Fig. 14b and d). In Nahuelbuta, fractions of extractable Al
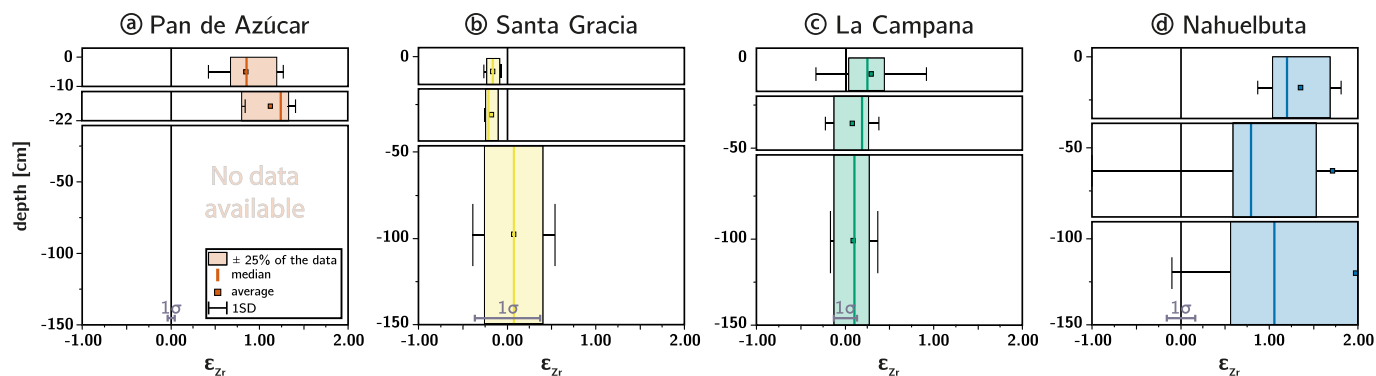
Fig. 13. Volumetric strain (ε) for each study sites' averaged A horizon (top), B horizon (middle) and saprolite (bottom) samples. Positive values denote to expansion and negative values to collapse of the regolith profile. See legend in panel a for the explanation of the uncertainty bars. The accuracy of the absolute ε values is limited by the variability in the respective sites' bedrock Zr concentration as indicated by the gray 1σ bar at the graphs' bottom. Note that the Y-axis scale is expanded by a factor of three for the A and B horizon in Pan de Azúcar. In this study site, no ε is available for the saprolite, as bulk density has not been determined for these samples.
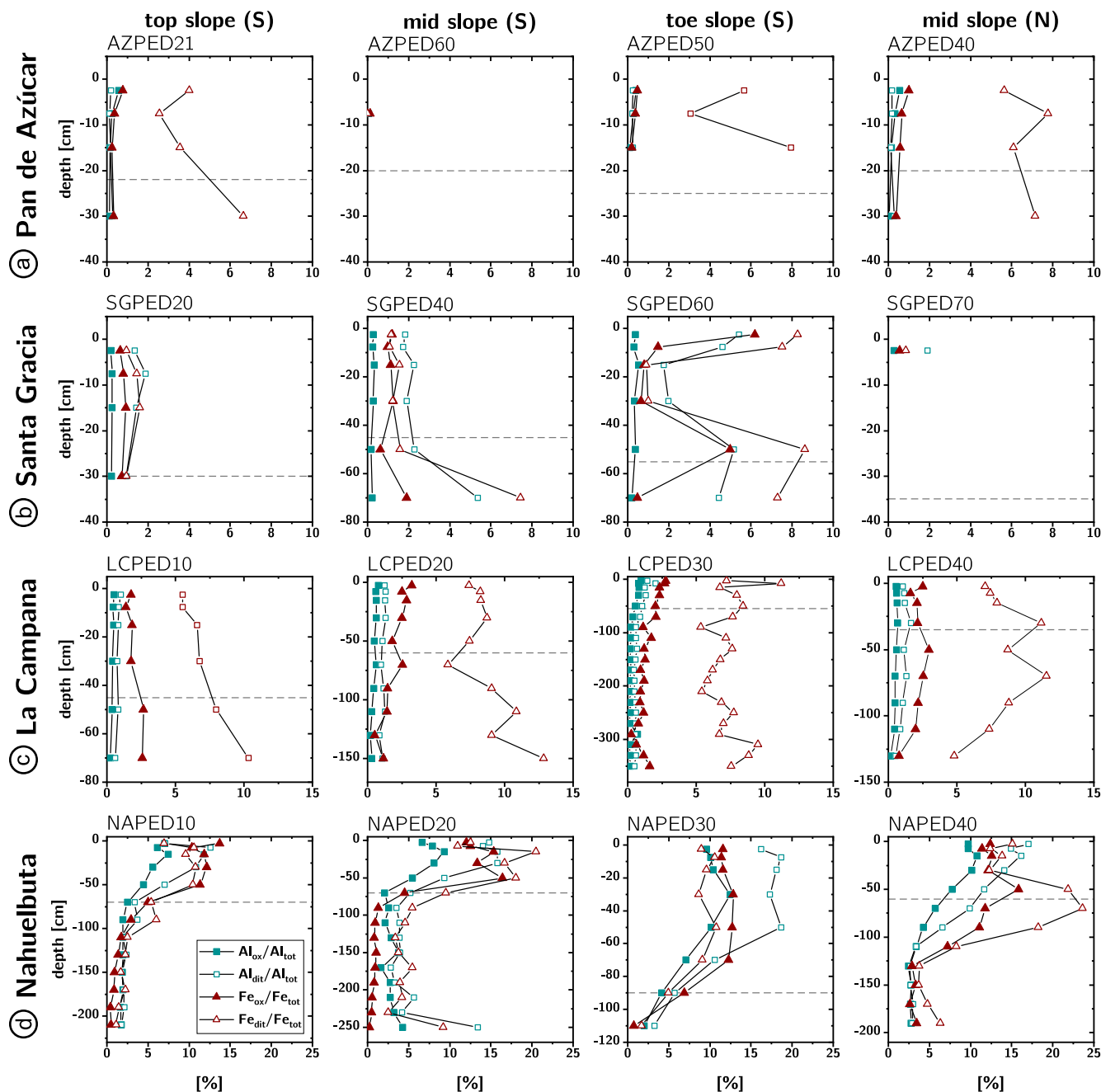
Fig. 14. Ratios of Al and Fe concentrations of the pedogenic oxide fraction (oxalate extracted, closed symbols; dithionite extract, open symbols) relative to total sample concentration. Regolith profile names are indicated above and dashed lines indicate the soil–saprolite boundary.

increase towards the profiles' A and B horizons. Here, the differences between oxalate- and dithionite-extractable fractions become increasingly pronounced. Pyrophosphate-extractable Al (Al_p, organic-bound colloidal Al) ranges from 30 to 12,500 ppm. Alike Fe_p, the highest absolute Al_p concentration is observed in Nahuelbuta.

Only small amounts of Si were extracted by oxalate (Si_o), dithionite (Si_d), and pyrophosphate (Si_p). Oxalate-extractable Si ranges from 65 to 1500 ppm, dithionite-extractable Si ranges from 65 to 3800 ppm, and pyrophosphate-extractable Si ranges from values below detection limit to 1615 ppm, respectively (Table S4). For all fractions, lowest values are observed in Pan de Azúcar (with the exception of Si_p in La Campana) and highest values are observed in Nahuelbuta. The oxalate-extractable Mn (Mn_o), dithionite-extractable Mn (Mn_d), and pyrophosphate-extractable Mn (Mn_p) range from 36 to 1400 ppm, from 22 to 1600 ppm, and from 1 to 420 ppm, respectively (Table S4).

5.4. Denudation, weathering, and erosion rates

In situ-produced ^{10}Be concentrations in quartz used for denudation rate calculations range between 8.9 ± 0.4 and $45.0 \pm 1.4 \times 10^4$ atoms g_{Qtz}^{-1} (Table S6). Denudation rates D calculated from these nuclide concentrations increase from Pan de Azúcar (S-facing: $11.0 \pm 0.7\,t\,km^{-2}\,yr^{-1}$; N-facing: $8.2 \pm 0.5\,t\,km^{-2}\,yr^{-1}$) to Santa Gracia (S-facing: $22.4 \pm 1.5\,t\,km^{-2}\,yr^{-1}$; N-facing: $15.9 \pm 0.9\,t\,km^{-2}\,yr^{-1}$) and La Campana (S-facing: $53.7 \pm 3.4\,t\,km^{-2}\,yr^{-1}$; N-facing: $69.2 \pm 4.6\,t\,km^{-2}\,yr^{-1}$). D at the southernmost location, Nahuelbuta, is lower than that at La Campana (S-facing: $47.5 \pm 3.0\,t\,km^{-2}\,yr^{-1}$; N-facing: $17.7 \pm 1.1\,t\,km^{-2}\,yr^{-1}$; Table S6).

Based on denudation rates and the CDF derived from Zr concentrations in soil and bedrock samples, respectively, the chemical
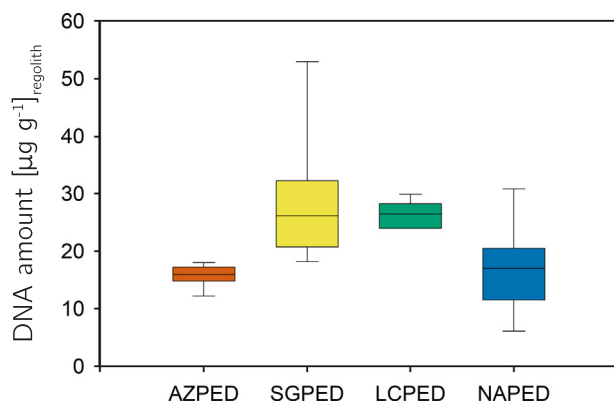
Fig. 15. Concentration of extracted DNA, averaged over the entire sampled saprolite depth. Box plots represent the sum of values of all topographic positions combined in Nahuelbuta (NAPED), La Campana (LCPED), Santa Gracia (SGPED) and Pan de Azúcar (AZPED). Median lines are indicated within the boxes of which the size corresponds to ± 25% of the data, whereas the whiskers show ± 1 st dev of all data. DNA was extracted from saprolite samples in triplicates.

weathering rate and the physical erosion rate are calculated using Eqs. (6) and (8) (Table S6). The average chemical weathering rates increase from Pan de Azúcar ($\approx 0.9\,\mathrm{t\,km^{-2}\,yr^{-1}}$; excluding the negative W value for AZPED21) to Santa Gracia ($\approx 9.5\,\mathrm{t\,km^{-2}\,yr^{-1}}$) and La Campana ($\approx 32.8\,\mathrm{t\,km^{-2}\,yr^{-1}}$). The physical erosion rate is similar in Pan de Azúcar and Santa Gracia (≈ 10.1 and $\approx 9.6\,\mathrm{t\,km^{-2}\,yr^{-1}}$), whereas the physical erosion rate is higher in La Campana ($\approx 28.7\,\mathrm{t\,km^{-2}\,yr^{-1}}$) than at the locations further North. The heterogeneity in bedrock and regolith Zr concentrations prohibits the calculation of an accurate weathering rate at Nahuelbuta. Taking the total denudation rates at face value, the estimated chemical weathering rates in Nahuelbuta would be $\approx 5.5\,\mathrm{t\,km^{-2}\,yr^{-1}}$ and the physical erosion rates would be $\approx 27.1\,\mathrm{t\,km^{-2}\,yr^{-1}}$. However, we have no confidence in the accuracy of these estimates.

5.5. Microbial abundance in saprolite

The extraction of total genomic DNA resulted in high variability (Fig. 15). Lowest DNA amounts were detected in saprolites from Pan de Azúcar with a minimum of $14.5 \pm 2.5\,\mathrm{\mu g\,g_{regolith}^{-1}}$, followed by

Nahuelbuta ranging from 14.0 ± 1.0 to $26.0 \pm 2.0\,\mathrm{\mu g\,g_{regolith}^{-1}}$. In contrast, highest DNA yields and variations from 20.5 ± 0.5 to $44.1 \pm 11.1\,\mathrm{\mu g\,g_{regolith}^{-1}}$ were obtained in saprolites from Santa Gracia. DNA concentration in La Campana mainly varied around $27.0\,\mathrm{\mu g\,g_{regolith}^{-1}}$ (Table S7).

Quantification of 16S rRNA genes revealed consistently higher abundances of bacteria than archaea within the saprolite samples (Fig. 16). Pan de Azúcar was the only primary study site with no topography-specific variations. Bacterial cell numbers ranged constantly around 10^5 gene copy numbers per gram of regolith. Archaea were lower by up to two orders of magnitude. Saprolites from Santa Gracia revealed the overall highest bacterial abundances in the top slope with 6.5×10^7 gene copies $\mathrm{g_{regolith}^{-1}}$. The lowest bacterial cell numbers with 3.9×10^4 copy numbers $\mathrm{g_{regolith}^{-1}}$ were detected in the mid-slope (N) in La Campana. In Nahuelbuta, the highest and lowest archaeal abundances were obtained, ranging from 1.2×10^2 in the mid-slope (S) to 5.2×10^6 gene copy numbers $\mathrm{g_{regolith}^{-1}}$ in the toe-slope. However, relative microbial abundances did not significantly differ between the regions Nahuelbuta, La Campana, and Santa Gracia ($P > 0.09$). Only data from Pan de Azúcar turned out to be significantly different from all other study sites ($P < 0.05$). In general, bacteria outnumber archaea in all study sites. In the driest regions Santa Gracia and Pan de Azúcar, the highest archaea-to-bacteria ratios were detected (Table S7). The overall highest archaea-to-bacteria ratio (1:217) was obtained in the mid-slope (N) in Santa Gracia. The mid-slope (S) of La Campana showed the lowest archaea-to-bacteria ratio (1:3).

6. Discussion

Assuming that the EarthShape approach, namely that geological boundary conditions (i.e. bedrock, rock uplift rate) do not differ along the transect, the bio-climatic forcings can be evaluated. We initiate this evaluation by structuring the observed geochemical trends into three categories: (1) A continental latitudinal trend, where (chemical) weathering intensity increases from north to south as precipitation and vegetation cover increase; (2) a local trend, where regolith on the N-facing catenae is exposed to more incoming solar radiation and thus less moisture is available for weathering reactions and plant biomass compared to the S-facing slope, and (3) an in-situ trend, where weathering intensity decreases with increasing regolith depth. We discuss these trends for the four EarthShape study sites. Further, we discuss the drivers of weathering and whether it is possible to discern abiotic from biotic processes.
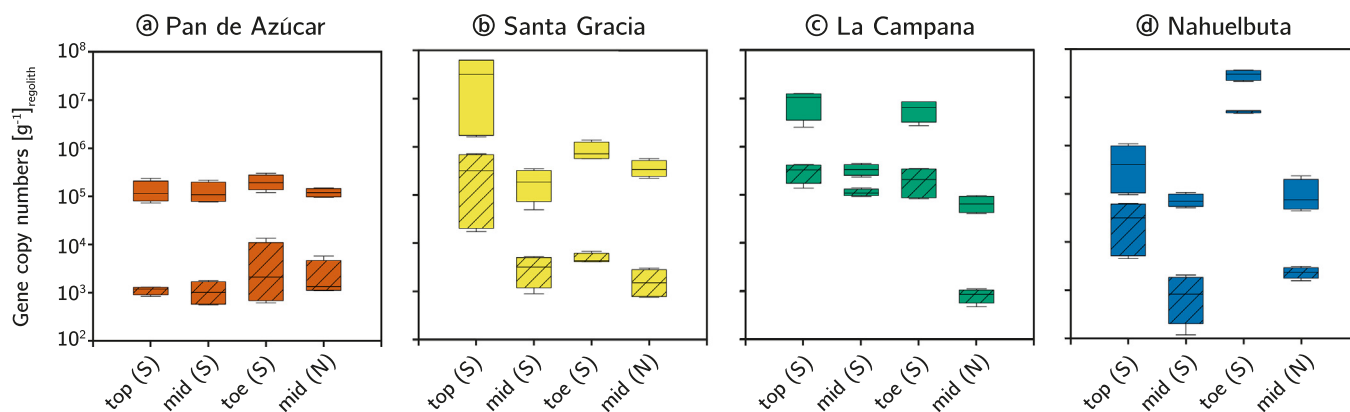
Fig. 16. Abundance of bacterial (open) and archaeal (patterned boxes) 16S rRNA gene copy numbers per gram of regolith in the primary study sites, averaged over the entire sampled saprolite depth. Saprolite samples were collected along the hillslope catena at four different positions. Box plots represent the sum of all replicate samples, each measured in quadruplicate qPCR reactions. Median lines are indicated within the boxes of which the size corresponds to ± 25% of the data, whereas the whiskers show ± 1 st dev of all data. S = south facing, N = north facing.

6.1. The continental trend

6.1.1. Permanent slow erosion: denudation rates and saprolite residence times

Total denudation rates increase from Pan de Azúcar (8–$11 \, \text{t km}^{-2} \, \text{yr}^{-1}$) to Santa Gracia ($16$–$22 \, \text{t km}^{-2} \, \text{yr}^{-1}$) and reach a maximum in La Campana (54–$69 \, \text{t km}^{-2} \, \text{yr}^{-1}$). Although MAP (Fig. 2) and vegetation cover increase from north to south, the denudation rate in Nahuelbuta is lower (18–$48 \, \text{t km}^{-2} \, \text{yr}^{-1}$; Table S6) than in La Campana. If not caused by a differing influence of biota on denudation processes (Schaller et al., 2018) between La Campana and Nahuelbuta, the difference in denudation rate between the two sites can be explained with (1) the hillslopes in La Campana that are the steepest of all study sites (Table S1); and (2) higher uplift rates in the region of La Campana compared to the other parts of the Chilean Coastal Cordillera (Carretier, 2018; Carretier et al., 2013), both leading to higher denudation rates. The denudation rates of this study are in agreement with published data. Owen et al. (2011) reported average bedrock erosion rates of active slopes from locations near Pan de Azúcar and Santa Gracia of $2.7 \pm 0.4 \, \text{mm} \cdot \text{ky}^{-1}$ and $26 \pm 7 \, \text{mm} \cdot \text{ky}^{-1}$, respectively. Based on a bedrock density of $\rho = 2.6 \, \text{g} \cdot \text{cm}^{-3}$, these rates equal a denudation rate of $\sim 7 \, \text{t km}^{-2} \, \text{yr}^{-1}$ and $\sim 70 \, \text{t km}^{-2} \, \text{yr}^{-1}$, respectively. At a location 50 km south from La Campana, the total denudation rates range from 42 to $147 \, \text{t km}^{-2} \, \text{yr}^{-1}$ (Vázquez et al., 2016), which encompasses our value of $60 \, \text{t km}^{-2} \, \text{yr}^{-1}$. All these rates are at the lower end of global cosmogenic nuclide-based soil denudation rates (Dixon and von Blanckenburg, 2012). The relative uniformity and narrow range can be attributed to the uniform tectonic drivers in the whole study area (Blanco-Chao et al., 2014; Melnik, 2016). Furthermore, the low denudation rates in the two northern sites are typical for those observed in arid areas (e.g. Carretier et al., 2015; Cockburn et al., 1999; Kober et al., 2007; Starke et al., 2017).

Residence times of material in the uppermost 60 cm of regolith (which is the cosmic ray mean attenuation pathway, used by convention to report residence times based on cosmogenic nuclides; von Blanckenburg, 2005) and the denudation rate are around 200 kyr in Pan de Azúcar, 100 kyr in Santa Gracia, 30 kyr in La Campana, and 40 to 100 kyr in Nahuelbuta. Thus, over these averaging time scales, the material contained in a 60 cm depth interval of regolith is being replaced by supply of material from depth, its removal by erosion at the surface, and weathering in the weathering zone. The regolith is thus permanently turned over by slow erosion.

6.1.2. Degree of weathering

Prior to comparing the degree of weathering between the four study sites, differences in their bedrock composition and potential external inputs have to be evaluated. All study sites are underlain by granitoid rock. However, its composition differs between sites. Bedrock at Pan de Azúcar and La Campana is granodioritic, bedrock at Santa Gracia is more mafic, ranging to quartz gabbro, and Nahuelbuta is intermediate with tonalitic composition (Fig. 7).

External input in the form of volcanic ash potentially affects Nahuelbuta, given the sites' proximity to the Andean volcanic arc (Moreno and Clavero Ribes, 2006; Naranjo and José, 2005; Parada et al., 2007; Petit-Breuilh and Lobato, 1994). Volcanic input results in soils with andic properties. Andic soils are defined to exist if the bulk density is typically lower than $0.9 \, \text{g cm}^{-3}$, $Al_o + 1/2 \, Fe_o$ exceeds a value of 0.4 or 2% (Bäumler et al., 2005, and references therein; Parfitt and Clayden, 1991), and a considerable amount of glass is found in the soil fraction $< 2 \, \text{mm}$ (i.e. $< 30\%$; Soil Survey Staff, 1999). The formation of allophane and imogolite would emerge if these glasses weather and ultimately lead to Si_o/Al_o ratios between 0.5 and 1 (Wada, 1989). In the soils of Nahuelbuta, bulk density is close to the threshold of $0.9 \, \text{g cm}^{-3}$ or below (Bernhard et al., 2018) and $Al_o + 1/2 \, Fe_o$ ratios exceed 0.4% persistently. However, $Al_o + 1/2 \, Fe_o > 2\%$ were never attained (Table S4) and no volcanic glass particles were found. Thus,
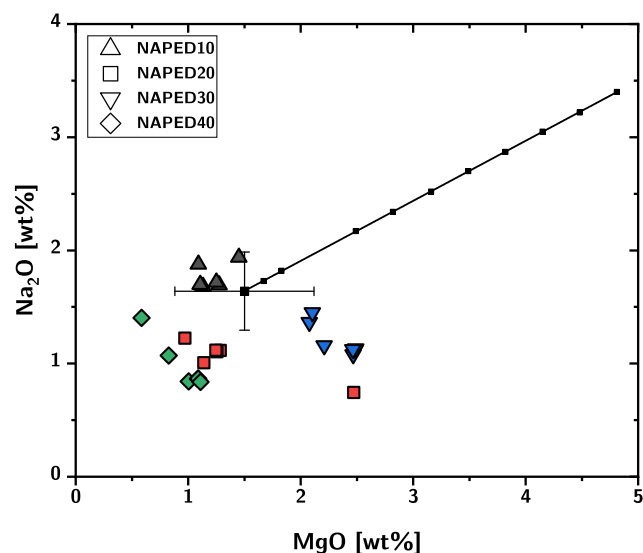
Fig. 17. Mixing model between average Na and Mg concentrations of Nahuelbuta saprolites (Na_2O: 1.64 wt% and MgO: 1.50 wt%) and andesitic ash (Na_2O: 3.40 wt% and MgO: 4.81 wt%), respectively. The black line represents the mixing line between 0% volcanic ash input to the left and 100% volcanic ash input to the right. Symbols represent samples from the A and B horizons at Nahuelbuta. The model indicates that the contribution of ash at the Nahuelbuta site is, if existing at all, insignificant.

the soils of Nahuelbuta reveal some features of andic soils. Still, neither the chemical composition of the investigated regolith samples nor the pedogenic oxides indicate the presence of volcanic ash: (1) No enrichment in Na, K, or Mg is observed in A or B horizons in any regolith profile. Mixing models between characteristic Mg and Na concentrations in andesitic volcanic ash and the Nahuelbuta saprolite indicate that volcanic ash additions, if occurring in soil, are insignificant and within the resolution of the sample, and are thus $< 2\%$ (Fig. 17); (2) Si_o/Al_o ratios are < 0.25; and (3) prevailing west winds (García, 1994) would impede the deposition of thick volcanic ash layers in this area.

The input of sea spray into the soil profiles is well-documented only at Pan de Azúcar by (1) lower CIA values in regolith than in bedrock (Fig. 9), (2) positive τ_{Ca} and τ_{Mg} (Fig. 12), and (3) further supported by positive ε (Fig. 13) despite CDF being close to zero (Fig. 12) in the soil horizons.

In granitoid rock, the maximum degree of weathering (CDF) is typically 50%, as the remaining mass is insoluble quartz and clay minerals (Hewawasam et al., 2013). Such maximum CDF would correspond to a CIA of 1. In Pan de Azúcar, physical erosion exceeds chemical weathering by an order of magnitude (Table S6). Here, the processes disintegrating rock and developing regolith are mainly physical weathering (CDF ≈ 0.1 over the entire profile; Fig. 11) and are mostly attributed to either insolation- or salt weathering, or a combination of both. This is also in agreement with the low abundance of microorganisms in the saprolite at this site. Upon insolation weathering, diurnal or annual heating and cooling cycles lead to a granular disintegration of biotite and to the grussification of feldspar and quartz. This process opens pathways along grain boundaries and ultimately increases the reactive surface of rock (e.g. Tchakerian and Pease, 2015; and references therein). Sea spray in combination with coastal fog (i.e. *camanchaca*) provides considerable amounts of water (e.g. Larrain et al., 2002). Consequently, the formation of gypsum and anhydrite (Fig. 3) further fracture the rock (i.e. salt weathering) and percolating moisture and oxygen initiate biotite weathering. These processes release approximately 8 to 10% of the total Fe from primary minerals and form secondary phases (Fig. 14). In Santa Gracia, chemical weathering equals physical erosion (Table S6). The high degree of weathering (CDF ≈ 0.4–0.5; Fig. 11) despite low precipitation can be attributed to

the low abundance of quartz on the one and the high abundance of weatherable plagioclase and mafic minerals on the other hand (Fig. 9; Table S3). However, given the high uncertainty in the bedrocks' Zr content and arising CDF uncertainties, we cannot exclude that the fraction of chemical weathering on total denudation is lower in this study site. In La Campana, chemical weathering also equals physical erosion (Table S6). Such a degree of weathering (CDF ≈ 0.3–0.6; Fig. 11) is expected in such a Mediterranean climate (e.g. Schoonejans et al., 2016). However, Al is also lost as indicated by negative τ values (Table S5). Thus, secondary mineral formation seems to be subordinate (Fig. 9). In Nahuelbuta, physical erosion outpaces chemical weathering by a factor of 5 (Table S6). However, we are unable to assign reliable ratios of erosion to weathering due to the high heterogeneity in bedrock and regolith samples.

Concentrations of oxalate- and dithionite-extractable Fe and Al (relative to the samples' Fe and Al content; Fig. 14) are increasing with increasing precipitation. Together, the proportion of well-crystallized Fe oxides (e.g. goethite, lepidocrocite, hematite) in the extractable Fe decreases with increasing precipitation (Fe_o/Fe_d; Table S4). These observations are in accordance with (1) chemical pedogenic development that is higher in humid climates compared to arid climates and, hence, a higher production rate of pedogenic Fe oxides and hydroxides (Alexander, 1985; Birkeland et al., 1989) and (2) a higher proportion of oxalate extractable oxides under more humid and, hence, higher soil moisture conditions (Schwertmann, 1964, 1985).

Regolith density in saprolite is another indicator of the degree of weathering. Along the transect, saprolite density (Bernhard et al., 2018) is 1.5–1.7 g cm^{-3} in Santa Gracia, 1.4–1.8 g cm^{-3} in La Campana, and 0.9–1.3 g cm^{-3} in Nahuelbuta (Table S4). In Pan de Azúcar, no volumetric samples were taken from the hard saprolite. By comparison, typical density in saprolites measured in weathering studies over granitoid rock in a range of denudation and climate zones are 1.0–1.5 g cm^{-3} in deep, slow humid tropical weathering, 1.3–2.5 g cm^{-3} in tropical granite rejuvenated by constant erosion, and 2.0–2.6 g cm^{-3} in rapidly eroding temperate climate (Anderson et al., 2002; Braun et al., 2009; Brimhall et al., 1991; Buss et al., 2017; Buss et al., 2008; Hewawasam et al., 2013; Scholten et al., 1997; White, 2002). Within uncertainties, the volumetric strain ε is zero in saprolite samples from Santa Gracia and La Campana (Fig. 13b, c). In Nahuelbuta ε, in saprolite largely scatters around its median value of about 1 (Fig. 13d). However, this scatter arises from the high variation of Zr within the regolith profile and is not necessarily related to expansion upon the formation of secondary minerals. Consequently, the EarthShape transect is subject to strong isovolumetric weathering despite strong differences in mass loss.

6.2. The local trend: N-facing versus S-facing hillslopes

The A and B horizons are thicker (with the exception of Pan de Azúcar) on S-facing slopes (Table S1), which is expected on N-facing slopes in the southern hemisphere as they are more prone to solar radiation and therefore experience more xeric conditions (Dixon, 2015). Still, neither in chemical property nor in the derived depletion indices (i.e. CDF & τ) we find significant differences between regolith profiles on N- and S-facing slopes. Additionally, pedogenic oxides neither differ significantly in (1) their total abundance, nor (2) their proportion of oxalate-extractable oxides, nor (3) their degree of chemical pedogenic development between regolith profiles on N- and S-facing slopes throughout all four study sites (Table S4).

In the two northern sites Pan de Azúcar and Santa Gracia, where solar inclination is high, the differences in microclimate and hence changes in vegetation cover and type between N- and S-facing slopes are minimal. Still, each combination of different (micro-) climate and biota might result in discernable weathering patterns. Thus, emerging differences in the weathering pattern in these sites might either not exist or might not be resolvable with the analyzes we applied. However,

the absence of significant differences in La Campana and Nahuelbuta is particularly surprising given the substantial differences in the vegetation and species composition between the N- and S-facing slopes in these sites. If the exposure to sunlight indeed controls biomass growth, then the absence of N–S differences in the degree of weathering and other chemical pedogenic properties could indicate that either the differences in vegetation between slopes are not big enough to be reflected on regolith processes, or that the impact of biogenic weathering in these four study sites is low.

La Campana was the only site showing N–S differences in bacterial and archaeal gene copies in saprolite. Archaea- to bacteria ratios differed among slopes in all sites, but showing contrasting patterns in different sites. In the saprolite on S-facing slopes of the Pan de Azúcar and Nahuelbuta region, bacteria are outnumbering archaea by far. In La Campana and Santa Gracia, this trend is seen in the saprolite on the N-facing slopes.

6.3. The in-situ trend: vertical structure of the weathering zone

Along the gradient the degree of soil formation increased with precipitation and vegetation cover (Bernhard et al., 2018) as shown by increasing thickness of soil horizons and an increasing amount of oxalate- and dithionite-leachable Al and Fe (Fig. 14, Tables S1 & S4). However, neither do total denudation rates nor the degree of weathering regularly increase with precipitation and vegetation cover. We cannot establish whether this observation also holds for the depth of the weathering zone, because in none of the regolith profiles the weathering front has been encountered. As our profiles attain a depth of 2 m at the most, this observation is expected as global depth profiling in weathered granitoid rock resulted in a mean depth of 13 ± 5 m for the location of the weathering front (i.e. where rock is converted into saprolite; Bazilevskaya et al., 2013). In the Chilean Coastal Cordillera, this depth appears to be even higher, exceeding 30 m in some cases (Vázquez et al., 2016). Such great depth, if not due to an inherited weathering history, could also be explained with the overall low erosion rates that prevents a steady state between weathering front advance rate and erosion at the surface (Lebedeva et al., 2010).

Within the sampled regolith profiles, vertical gradients are virtually absent within the saprolite. This stability hints at a depletion gradient that is located at a much greater depth. However, gradients in elemental concentrations and depletion do appear within the soil horizons. Namely, P concentrations increase over those found in the saprolite in all sites, and strongly so in Nahuelbuta. This increase hints at nutrient uplift and recycling via leaf and root litter (Jobbagy and Jackson, 2004). Vertical gradients in element depletion are not discernable due to the high initial bedrock heterogeneity.

That the depth profiles of pedogenic oxides show a relative decrease in pedogenic to total oxide ratios in Nahuelbuta and to a lesser extend in La Campana can be interpreted to be caused by gradients in regolith moisture. For the other two sites, there is no clear decrease of this ratio with depth, which can be explained by the lower infiltration into these profiles.

Total microbial abundances decrease with depth at all study sites, containing the highest abundances in surface soils as shown in (Bernhard et al., 2018). This pattern is in agreement with several other studies, which highlight the importance of soil depth and plant C input on microbial abundance and community structures (Agnelli et al., 2004; Eilers et al., 2012; Fierer et al., 2003; Will et al., 2010). Moreover, bacteria numerically dominate over archaea also in the saprolites in all sites.

6.4. Is the biogenic weathering engine discernable?

The coastal dry environments of northern Chile (from 20 to 32°S; Pan de Azúcar and Santa Gracia) are characterized by permanently low water availability and biotic activities that are controlled by rare

episodic moisture inputs (Armesto et al., 2007; Rundel et al., 2007). Samples from these two sites show no significant element depletion in the soil compared to the saprolite (Figs. 11 & 12). In the samples from Nahuelbuta, which receive the largest amount of annual rainfall, elements such as Ca, Mg, K, and Na that do not form insoluble hydroxides and are readily leached, show the largest degree of depletion (Fig. 12). Thus, as a result of this increased leaching with increasing precipitation the pools of mineral-derived nutrients decrease along the precipitation gradient from north to south. Yet, at none of the sites the regolith is so depleted in mineral nutrients that the weathering zone would be "supply-limited". In the geochemical terminology, this means that nutritive elements are wholesale absent in regolith, which then depends on recycling and aeolian inputs (Dixon et al., 2012; Porder et al., 2007; Uhlig et al., 2017). The main imprint of biogenic processes we found to be the enrichment of P and partly Mg that can be observed in samples from the A- compared to the B-horizons at La Campana and Nahuelbuta (Fig. 12c, d). This surface enrichment shows that nutrient uplift and vegetation recycling is at work at those sites (e.g. Jobbagy and Jackson, 2004; Porder and Chadwick, 2009).

All sites do contain distinct bio-signatures though. Properties found in the A and B horizons of soils that can, in theory, be interpreted to be influenced by biota, such as total organic carbon content and C/N ratios show pronounced trends along the transect (Bernhard et al., 2018). In the saprolite, bacterial gene copies (indicative for universal abundances) are highest at the non-arid sites. Previous studies already indicated that deeper soil layers contain microbial communities, specialized for low C and O_2 input (Fritze et al., 2000; Ghiorse and Wilson, 1988; Zvyagintsev, 1994). This strategy to exploit different ecological niches is also provided by the interaction with soil minerals (Ehrlich, 1995). Several studies already demonstrated the crucial influence of minerals on the bacterial community structure (Carson et al., 2009; Carson et al., 2007; Certini et al., 2004). Thus, it is suggested that these microbes may provide a biological contribution to mineral-weathering processes.

7. Conclusions

We provided first interpretation of a comprehensive geochemical dataset, addressing how climate and vegetation cover influence weathering, microbial abundance and potential activity, and mineral nutrient supply to different ecosystems in the Chilean Coastal Cordillera. We explored four sites along a climate gradient from arid to humid with S-and N-facing regolith profiles that experienced low and high insolation, respectively. We provided a complete description of (1) the regolith profiles and their vegetation cover; (2) the denudation rates that describe their permanent turnover by erosion and weathering; (3) a comprehensive geochemical characterization of regolith and bedrock as well as (4) microbial abundances in the saprolite.

We found that denudation rates generally increase with increasing precipitation and vegetation cover from north to south, being highest in the Mediterranean climate of La Campana, where hillslopes are also highest. Further south in Nahuelbuta where precipitation and the vegetation cover are highest, denudation rates are lower than in La Campana. However, hillslopes in Nahuelbuta are also lower than in La Campana. These low slopes can explain the difference in denudation rate if it is not due to the higher vegetation cover. Chemical depletion and microbial abundances in saprolite are low in Pan de Azúcar (arid and sparsely vegetated site) and are higher in the three southern (more humid and denser vegetated) sites that do not show pronounced differences between them. However, no clear trend of chemical depletion and microbial abundances with increasing precipitation and vegetation cover has been found.

We have shown that the thickness of the soil horizons is higher on S-facing slopes compared to the N-facing analogues. However, expected differences in the degree of chemical weathering between S- and N-facing slopes could not be detected. Thus, the N–S comparison did not

yet allow to discern the effects of abiotic versus biotic weathering.

Even though indicators of weathering characteristics that allow to distinguish the abiotic (purely climate-related) from the biotic (climate- and bio-related) driver have not yet emerged, the EarthShape study sites are suited to evaluate biological effects on weathering, using advanced biological and geochemical techniques. Future studies should focus on the unique and puzzling features of the EarthShape Critical Zones such as (1) the low chemical weathering rates, which appear to be contradicted by the substantial depth of the weathering front; and (2) the interacting role of climate, vegetation, microbiota, and fauna in controlling the respective erosion and weathering rates. These findings will eventually be placed into the context of efforts to derive the abiotic and biotic driving forces that shape the Critical Zone, both within future studies in the "EarthShape" project, and within global studies of the Critical Zone (Brantley et al., 2016; Chorover et al., 2007; Hilton, 2017; Riebe et al., 2017).

Acknowledgements

References

Agnelli, A., Ascher, J., Corti, G., Ceccherini, M.T., Nannipieri, P., Pietramellara, G., 2004. Distribution of microbial communities in a forest soil profile investigated by microbial biomass, soil respiration and DGGE of total and extracellular DNA. Soil Biol. Biochem. 36, 859–868.

Alexander, E.B., 1985. Estimating relative ages from iron-oxide/total-iron ratios of soils in the Western Po Valley, Italy - a discussion. Geoderma 35, 257–259.

Amundson, R., Berhe, A.A., Hopmans, J.W., Olson, C., Sztein, A.E., Sparks, D.L., 2015a. Soil and human security in the 21st century. Science 348, 1261071.

Amundson, R., Heimsath, A., Owen, J., Yoo, K., Dietrich, W.E., 2015b. Hillslope soils and vegetation. Geomorphology 234, 122–132.

Anderson, S.P., Dietrich, W.E., Brimhall Jr., G.H., 2002. Weathering profiles, mass-balance analysis, and rates of solute loss linkages between weathering a small, steep catchment. Geol. Soc. Am. Bull. 114, 1143–1158.

Anderson, S.P., von Blanckenburg, F., White, A.F., 2007. Physical and chemical controls on the critical zone. Elements 3, 315–319.

Armesto, J.J., Vidiella, P.E., Gutiérrez, J.R., 1993. Plant communities of the fog-free coastal desert of Chile: plant strategies in a fluctuating environment. Rev. Chil. Hist. Nat. 66, 271–282.

Armesto, J.J., Arroyo, M.T., Hinojosa, L.F., 2007. The Mediterranean environment of central Chile. In: Veblen, T., Young, K., Orme, A. (Eds.), The Physical Geography of South America. Oxford Univ. Press, New York, pp. 184–199.

Bahre, C.J., 1979. Destruction of the Natural Vegetation of North-Central Chile. Univ of California Press.

Balogh-Brunstad, Z., Keller, C.K., Gill, R.A., Bormann, B.T., Li, C.Y., 2008. The effect of bacteria and fungi on chemical weathering and chemical denudation fluxes in pine growth experiments. Biogeochemistry 88, 153–167.

Bardelli, T., Gomez-Brandon, M., Ascher-Jenull, J., Fornasier, F., Arfaioli, P., Francioli, D., Egli, M., Sartori, G., Insam, H., Pietramellara, G., 2017. Effects of slope exposure on soil physico-chemical and microbiological properties along an altitudinal climosequence in the Italian Alps. Sci. Total Environ. 575, 1041–1055.

Barnes, J.B., Ehlers, T.A., 2009. End member models for Andean Plateau uplift. Earth Sci. Rev. 91, 105–132.

Bäumler, R., Caspari, T., Totsche, K.U., Dorji, T., Norbu, C., Baillie, I.C., 2005. Andic properties in soils developed from nonvolcanic materials in Central Bhutan. J. Plant Nutr. Soil Sci. 168, 703–713.

Bazilevskaya, E., Lebedeva, M., Pavich, M., Rother, G., Parkinson, D.Y., Cole, D., Brantley, S.L., 2013. Where fast weathering creates thin regolith and slow weathering creates thick regolith. Earth Surf. Process. Landf. 38, 847–858.

Bernhard, N., Moskwa, L.-M., Schmidt, K., Oeser, R.A., Aburto, F., Bader, M.Y., Baumann, K., von Blanckenburg, F., Boy, J., van den Brink, L., Brucker, E., Canessa, R., Dippold, M.A., Ehlers, T.A., Fuentes, J.P., Godoy, R., Köster, M., Kuzyakov, Y., Leinweber, P., Neidhard, H., Matus, F., Mueller, C.W., Oelmann, Y., Oses, R., Osses, P., Paulino, L., Schaller, M., Schmid, M., Spielvogel, S., Spohn, M., Stock, S., Stroncik, N., Tielbörger, K., Übernickel, K., Scholten, T., Seguel, O., Wagner, D., Kühn, P., 2018. Pedogenic and microbial interrelations to regional climate and local topography: new insights from a climate gradient (Arid to Humid) along the Coastal Cordillera of Chile. Catena 170, 335–355. http://dx.doi.org/10.1016/j.catena.2018.06.018.

Birkeland, P.W., Burke, R.M., Benedict, J.B., 1989. Pedogenic gradients for Iron and aluminum accumulation and phosphorus depletion in Arctic and Alpine soils as a function of time and climate. Quart. Res. 32, 193–204.

Blanco-Chao, R., Pedoja, K., Witt, C., Martinod, J., Husson, L., Regard, V., Audin, L., Nexer, M., Delcaillau, B., Saillard, M., Melnick, D., Dumont, J.F., Santana, E., Navarrete, E., Martillo, C., Pappalardo, M., Ayala, L., Araya, J.F., Feal-Perez, A., Correa, D., Arozarena-Llopis, I., 2014. The rock coast of South and Central America. In: Rock Coast Geomorphology: A Global Synthesis. 40. pp. 155–191.

Bojko, O., Kabala, C., 2017. Organic carbon pools in mountain soils — sources of variability and predicted changes in relation to climate and land use changes. Catena 149, 209–220.

Borchers, B., Marrero, S., Balco, G., Caffee, M., Goehring, B., Lifton, N., Nishiizumi, K., Phillips, F., Schaefer, J., Stone, J., 2016. Geological calibration of spallation production rates in the CRONUS-Earth project. Quat. Geochronol. 31, 188–198.

Brantley, S.L., Megonigal, J.P., Scatena, F.N., Balogh-Brunstad, Z., Barnes, R.T., Bruns, M.A., Van Cappellen, P., Dontsova, K., Hartnett, H.E., Hartshorn, A.S., Heimsath, A., Herndon, E., Jin, L., Keller, C.K., Leake, J.R., McDowell, W.H., Meinzer, F.C., Mozdzer, T.J., Petsch, S., Pett-Ridge, J., Pregitzer, K.S., Raymond, P.A., Riebe, C.S., Shumaker, K., Sutton-Grier, A., Walter, R., Yoo, K., 2011. Twelve testable hypotheses on the geobiology of weathering. Geobiology 9, 140–165.

Brantley, S.L., DiBiase, R.A., Russo, T.A., Shi, Y., Lin, H., Davis, K.J., Kaye, M., Hill, L., Kaye, J., Eissenstat, D.M., Hoagland, B., Dere, A.L., Neal, A.L., Brubaker, K.M., Arthur, D.K., 2016. Designing a suite of measurements to understand the critical zone. Earth Surf. Dyn. 4, 211–235.

Braucher, R., Merchel, S., Borgomano, J., Bourlès, D.L., 2011. Production of cosmogenic radionuclides at great depth: a multi element approach. Earth Planet. Sci. Lett. 309, 1–9.

Braun, J.-J., Descloitres, M., Riotte, J., Fleury, S., Barbiéro, L., Boeglin, J.-L., Violette, A., Lacarce, E., Ruiz, L., Sekhar, M., Mohan Kumar, M.S., Subramanian, S., Dupré, B., 2009. Regolith mass balance inferred from combined mineralogical, geochemical and geophysical studies: Mule Hole gneissic watershed, South India. Geochim. Cosmochim. Acta 73, 935–961.

Brimhall, G.H., Dietrich, W.E., 1987. Constitutive mass balance relations between chemical composition, volume, density, porosity, and strain in metasomatic hydrochemical systems: results on weathering and pedogenesis. Geochim. Cosmochim. Acta 51, 567–587.

Brimhall, G.H., Christopher, J.L., Ford, C., Bratt, J., Taylor, G., Warin, O., 1991. Quantitative geochemical approach to pedogenesis: importance of parent material reduction, volumetric expansion, and eolian influx in lateritization. Geoderma 51, 51–91.

Buss, H.L., Bruns, M.A., Schultz, D.J., Moore, J., Mathur, C.F., Brantley, S.L., 2005. The coupling of biological iron cycling and mineral weathering during saprolite formation, Luquillo Mountains, Puerto Rico. Geobiology 3, 247–260.

Buss, H.L., Sak, P.B., Webb, S.M., Brantley, S.L., 2008. Weathering of the Rio Blanco quartz diorite, Luquillo Mountains, Puerto Rico: coupling oxidation, dissolution, and fracturing. Geochim. Cosmochim. Acta 72, 4488–4507.

Buss, H.L., Chapela Lara, M., Moore, O.W., Kurtz, A.C., Schulz, M.S., White, A.F., 2017. Lithological influences on contemporary and long-term regolith weathering at the Luquillo Critical Zone Observatory. Geochim. Cosmochim. Acta 196, 224–251.

Carretier, S., 2018. Review of erosion dynamics along the major N-S climatic gradient in Chile and perspectives. Geomorphology 300, 45–68.

Carretier, S., Regard, V., Vassallo, R., Aguilar, G., Martinod, J., Riquelme, R., Pepin, E., Charrier, R., Hérail, G., Farías, M., Guyot, J.L., Vargas, G., Lagane, C., 2013. Slope and climate variability control of erosion in the Andes of central Chile. Geology 41, 195–198.

Carretier, S., Regard, V., Vassallo, R., Aguilar, G., Martinod, J., Riquelme, R., Christophoul, F., Charrier, R., Gayer, E., Farías, M., Audin, L., Lagane, C., 2015. Differences in 10Be concentrations between river sand, gravel and pebbles along the western side of the central Andes. Quat. Geochronol. 27, 33–51.

Carson, J.K., Rooney, D., Gleeson, D.B., Clipson, N., 2007. Altering the mineral composition of soil causes a shift in microbial community structure. FEMS Microbiol. Ecol. 61, 414–423.

Carson, J.K., Campbell, L., Rooney, D., Clipson, N., Gleeson, D.B., 2009. Minerals in soil select distinct bacterial communities in their microhabitats. FEMS Microbiol. Ecol. 67, 381–388.

Certini, G., Campbell, C.D., Edwards, A.C., 2004. Rock fragments in soil support a different microbial community from the fine earth. Soil Biol. Biochem. 36, 1119–1128.

Chadwick, O.A., Brimhall, G.H., Hendricks, D.M., 1990. From a black to a gray box — a mass balance interpretation of pedogenesis. Geomorphology 3, 369–390.

Charrier, R., Pinto, L., Rodríguez, M.P., 2007. Tectonostratigraphic evolution of the Andean Orogen in Chile. In: Moreno, T., Gibbons, W. (Eds.), The Geology of Chile. The Geological Society of London, pp. 21–114.

Chmeleff, J., von Blanckenburg, F., Kossert, K., Jakob, D., 2010. Determination of the 10Be half-life by multicollector ICP-MS and liquid scintillation counting. Nucl.

Instrum. Methods Phys. Res., Sect. B 268, 192–199.

Chorover, J., Kretzschmar, R., Garcia-Pichel, F., Sparks, D.L., 2007. Soil biogeochemical processes within the critical zone. Elements 3, 321–326.

Clarke, J.D.A., 2006. Antiquity of aridity in the Chilean Atacama Desert. Geomorphology 73, 101–114.

Cockburn, h.A.P., Seid, M.A., Summerfield, M.A., 1999. Quantifying denudation rates on inselbergs in the central Namib Desert using in situ–produced cosmogenic 10Be and 26Al. Geology 27, 399–402.

Dere, A.L., White, T.S., April, R.H., Reynolds, B., Miller, T.E., Knapp, E.P., McKay, L.D., Brantley, S.L., 2013. Climate dependence of feldspar weathering in shale soils along a latitudinal gradient. Geochim. Cosmochim. Acta 122, 101–126.

Dixon, J.C., 2015. Soil Morphology in the Critical Zone: The Role of Climate, Geology, and Vegetation in Soil Formation in the Critical Zone, Principles and Dynamics of the Critical Zone. Elsevier, pp. 147–172.

Dixon, J.L., von Blanckenburg, F., 2012. Soils as pacemakers and limiters of global silicate weathering. Compt. Rendus Geosci. 344, 597–609.

Dixon, J.L., Heimsath, A.M., Amundson, R., 2009. The critical role of climate and saprolite weathering in landscape evolution. Earth Surf. Process. Landf. 34, 1507–1521.

Dixon, J.L., Hartshorn, A.S., Heimsath, A.M., DiBiase, R.A., Whipple, K.X., 2012. Chemical weathering response to tectonic forcing: a soils perspective from the San Gabriel Mountains, California. Earth Planet. Sci. Lett. 323-324, 40–49.

Doughty, C.E., Taylor, L.L., Girardin, C.A., Makhi, Y., Beerling, D.J., 2014. Montane forest root growth and soil organic layer depth as potential factors stabilizing Cenozoic global change. Geophys. Res. Lett. 41, 983–990.

Dunai, T.J., González López, G.A., Juez-Larré, J., 2005. Oligocene–Miocene age of aridity in the Atacama Desert revealed by exposure dating of erosion-sensitive landforms. Geology 33, 321.

Egli, M., Mirabella, A., Sartori, G., Fitze, P., 2003. Weathering rates as a function of climate: results from a climosequence of the Val Genova (Trentino, Italian Alps). Geoderma 111, 99–121.

Egli, M., Mirabella, A., Mancabelli, A., Sartori, G., 2004. Weathering of soils in alpine areas as influenced by climate and parent material. Clay Clay Miner. 52, 287–303.

Egli, M., Dahms, D., Norton, K., 2014. Soil formation rates on silicate parent material in alpine environments: different approaches-different results? Geoderma 213, 320–333.

Ehlers, T.A., von Blanckenburg, F., Übernickel, K., 2017. EarthShape weather station data collection. Retrieved from https://esdynamics.geo.uni-tuebingen.de/earthshape/index.php?id=68.

Ehrlich, H.L., 1995. How microbes influence mineral growth and dissolution. Chem. Geol. 132, 5–9.

Eilers, K.G., Debenport, S., Anderson, S., Fierer, N., 2012. Digging deeper to find unique microbial communities: the strong effect of depth on the structure of bacterial and archaeal communities in soil. Soil Biol. Biochem. 50, 58–65.

Ferrier, K.L., Kirchner, J.W., Finkel, R.C., 2012. Weak influences of climate and mineral supply rates on chemical erosion rates: measurements along two altitudinal transects in the Idaho Batholith. J. Geophys. Res. Earth 117 (n/a-n/a).

Fierer, N., Schimel, J.P., Holden, P.A., 2003. Variations in microbial community composition through two soil depth profiles. Soil Biol. Biochem. 35, 167–176.

Fritze, H., Pietikäinen, J., Pennanen, T., 2000. Distribution of microbial biomass and phospholipid fatty acids in Podzol profiles under coniferous forest. Eur. J. Soil Sci. 51, 565–573.

Gaillardet, J., Dupré, B., Louvat, P., Allègre, C.J., 1999. Global silicate weathering and CO2 consumption rates deduced from the chemistry of large rivers. Chem. Geol. 159, 3–30.

Gajardo, R., 1994. La vegetación natural de Chile: clasificación y distribución geográfica. Editorial Universitaria, Santiago.

Gantner, S., Andersson, A.F., Alonso-Sáez, L., Bertilsson, S., 2011. Novel primers for 16S rRNA-based archaeal community analyses in environmental samples. J. Microbiol. Methods 84, 12–18.

García, N.O., 1994. South American climatology. Quat. Int. 21, 7–27.

Ghiorse, W.C., Wilson, J.T., 1988. Microbial ecology of the terrestrial subsurface. In: Laskin, A.I. (Ed.), Advances in Applied Microbiology. Academic Press, pp. 107–172.

Green, E., Dietrich, W., Banfield, J., 2006. Quantification of chemical weathering rates across an actively eroding hillslope. Earth Planet. Sci. Lett. 242, 155–169.

Hahm, W.J., Riebe, C.S., Lukens, C.E., Araki, S., 2014. Bedrock composition regulates mountain ecosystems and landscape evolution. Proc. Natl. Acad. Sci. U. S. A. 111, 3338–3343.

Heimsath, A.M., Dietrich, W.E., Nishiizumi, K., Finkel, R.C., 1997. The soil production function and landscape equilibrium. Nature 388, 358–361.

Hervé, F., Munizaga, F., Parada, M.A., Brook, M., Pankhurst, R.J., Snelling, N.J., Drake, R., 1988. Granitoids of the Coast Range of central Chile: geochronology and geologic setting. J. S. Am. Earth Sci. 1, 185–194.

Hervé, F., Faundez, V., Calderón, M., Massonne, H., Willner, A., 2007. Metamorphic and plutonic basement complexes. In: Moreno, T., Gibbons, W. (Eds.), The Geology of Chile. The Geological Society of London, pp. 5–19.

Hewawasam, T., von Blanckenburg, F., Bouchez, J., Dixon, J.L., Schuessler, J.A., Maekeler, R., 2013. Slow advance of the weathering front during deep, supply-limited saprolite formation in the tropical Highlands of Sri Lanka. Geochim. Cosmochim. Acta 118, 202–230.

Hilton, R.G., 2017. Climate regulates the erosional carbon export from the terrestrial biosphere. Geomorphology 277, 118–132.

Hulton, N.R.J., Purves, R.S., McCulloch, R.D., Sugden, D.E., Bentley, M.J., 2002. The Last Glacial Maximum and deglaciation in southern South America. Quat. Sci. Rev. 21, 233–241.

Jobbagy, E.G., Jackson, R.B., 2004. The uplift of soil nutrients by plants: biogeochemical consequences across scales. Ecology 85, 2380–2389.

Johannsen, A., 1937. A descriptive petrography of the igneous rocks. Geol. Foereningan Stockh. Foerhandlingar 59, 363–364.

Juez-Larré, J., Kukowski, N., Dunai, T.J., Hartley, A.J., Andriessen, P.A.M., 2010. Thermal and exhumation history of the Coastal Cordillera arc of northern Chile revealed by thermochronological dating. Tectonophysics 495, 48–66.

Jungers, M.C., Heimsath, A.M., Amundson, R., Balco, G., Shuster, D., Chong, G., 2013. Active erosion–deposition cycles in the hyperarid Atacama Desert of Northern Chile. Earth Planet. Sci. Lett. 371-372, 125–133.

Khomo, L., Hartshorn, A.S., Rogers, K.H., Chadwick, O.A., 2011. Impact of rainfall and topography on the distribution of clays and major cations in granitic catenas of southern Africa. Catena 87, 119–128.

Khomo, L., Bern, C.R., Hartshorn, A.S., Rogers, K.H., Chadwick, O.A., 2013. Chemical transfers along slowly eroding catenas developed on granitic cratons in southern Africa. Geoderma 202-203, 192–202.

Khormali, F., Ghergherechi, S., Kehl, M., Ayoubi, S., 2012. Soil formation in loess-derived soils along a subhumid to humid climate gradient, Northeastern Iran. Geoderma 179-180, 113–122.

Kober, F., Ivy-Ochs, S., Schlunegger, F., Baur, H., Kubik, P.W., Wieler, R., 2007. Denudation rates and a topography-driven rainfall threshold in northern Chile: multiple cosmogenic nuclide data and sediment yield budgets. Geomorphology 83, 97–120.

Korschinek, G., Bergmaier, A., Faestermann, T., Gerstmann, U.C., Knie, K., Rugel, G., Wallner, A., Dillmann, I., Dollinger, G., von Gostomski, C.L., Kossert, K., Maiti, M., Poutivtsev, M., Remmert, A., 2010. A new value for the half-life of 10Be by Heavy-Ion Elastic Recoil Detection and liquid scintillation counting. Nucl. Instrum. Methods Phys. Res., Sect. B 268, 187–191.

Larrain, H., Velásquez, F., Cereceda, P., Espejo, R., Pinto, R., Osses, P., Schemenauer, R.S., 2002. Fog measurements at the site "Falda Verde" north of Chañaral compared with other fog stations of Chile. Atmos. Res. 64, 273–284.

Le Bas, M.J., Le Maitre, R.W., Streckeisen, A.L., Zanettin, B., 1986. A chemical classification of volcanic rocks based on the total alkali-silica diagram. J. Petrol. 27, 745–750.

Lebedeva, M.I., Fletcher, R.C., Brantley, S.L., 2010. A mathematical model for steady-state regolith production at constant erosion rate. Earth Surf. Process. Landf. 35, 508–524.

Lifton, N.A., Sato, T., Dunai, T.J., 2014. Scaling in situ cosmogenic nuclide production rates using analytical approximations to atmospheric cosmic-ray fluxes. Earth Planet. Sci. Lett. 386, 149–160.

Luebert, F., Pliscoff, P., 2006. Sinópsis bioclimática y vegetacional de Chile. Editorial Universitaria, Santiago de Chile.

Marrero, S.M., Phillips, F.M., Borchers, B., Lifton, N., Aumer, R., Balco, G., 2016. Cosmogenic nuclide systematics and the CRONUScalc program. Quat. Geochronol. 31, 160–187.

Marticorena, C., Quezada, M., 1985. Catálogo de la flora vascular de Chile. Gayana Bot. 42, 5–157.

Mehra, O.P., Jackson, M.L., 1958. Iron oxide removal from soils and clays by a dithionite-citrate system buffered with sodium bicarbonate. Natl. Conf. Clays Clays Miner. 317–327.

Melnik, D., 2016. Rise of the central Andean coast by earthquakes straddling the Moho. Nat. Geosci. 9, 401–407.

Ministerio de Obras Públicas, M, 2017. Información Oficial Hidrometeorológica y de Calidad de Aguas en Línea. In: DGA.

Moreno, H., Clavero Ribes, J., 2006. Geología del Volcán Villarrica - Regiones de La Araucanía y de Los Lagos, Carta Geológica de Chile, Serie Geología Básica No. 98. In: Sernageomin.

Moscoso, R., Nasi, C., Salinas, P., 1982. Hoja Vallenar y parte norte de La Serena: regiones de Atacama y Coquimbo: carta geológica de Chile 1:250.000. Servicio Nacional de Geología y Minería Chile.

Muyzer, G., De Waal, E.C., Uitterlinden, A.G., 1993. Profiling of complex microbial populations by denaturing gradient gel electrophoresis analysis of polymerase chain reaction-amplified genes coding for 16S rRNA. Appl. Environ. Microbiol. 59, 695–700.

Naranjo, S., José, A., 2005. Geología del Volcán Llaima, Región de La Araucanía, Escala: 1:50.000, Carta Geológica de Chile, Serie Geología Básica n°88, Santiago. Servicio Nacional de Geología y Minería.

Nesbitt, H.W., Young, G.M., 1982. Early Proterozoic climates and plate motions inferred from major element chemistry of lutites. Nature 299, 715–717.

Oeser, R.A., Stroncik, N., Moskwa, L.-M., Bernhard, N., Schaller, M., Canessa, R., van den Brink, L., Köster, M., Brucker, E., Stock, S., Fuentes, J.P., Godoy, R., Matus, F.J., Oses Pedraza, R., Osses McIntyre, P., Paulino, L., Seguel, O., Bader, M.Y., Boy, J., Dippold, M.A., Ehlers, T.A., Kühn, P., Kuzyakov, Y., Leinweber, P., Scholten, T., Spielvogel, S., Spohn, M., Übernickel, K., Tielbörger, K., Wagner, D., von Blanckenburg, F., 2018. Data supplement to: chemistry and microbiology of the Critical Zone along a steep climate and vegetation gradient in the Chilean Coastal Cordillera. In: GFZ Data Services, http://dx.doi.org/10.5880/GFZ.3.3.2018.001.

Owen, J.J., Amundson, R., Dietrich, W.E., Nishiizumi, K., Sutter, B., Chong, G., 2011. The sensitivity of hillslope bedrock erosion to precipitation. Earth Surf. Process. Landf. 36, 117–135.

Pagani, M., Caldeira, K., Berner, R., Beerling, D.J., 2009. The role of terrestrial plants in limiting atmospheric CO_2 decline over the past 24 million years. Nature. http://dx.doi.org/10.1038/nature08133.

Pankhurst, R.J., Hervé, F., 2007. Introduction and overview. In: Moreno, T., Gibbons, W. (Eds.), The Geology of Chile. The Geological Society of London.

Parada, M.A., Rivano, S., Sepulveda, P., Herve, M., Herve, F., Puig, A., Munizaga, F., Brook, M., Pankhurst, R., Snelling, N., 1988. Mesozoic and cenozoic plutonic development in the Andes of central Chile (30°30′–32°30′S). J. S. Am. Earth Sci. 1,

249–260.

Parada, M.A., Nyström, J.O., Levi, B., 1999. Multiple sources for the Coastal Batholith of central Chile (31–34°S): geochemical and Sr–Nd isotopic evidence and tectonic implications. Lithos 46, 505–521.

Parada, M.A., López-Escobar, L., Oliveros, V., Fuentes, F., Morata, D., Calderón, M., Aguirre, L., Féraud, G., Espinoza, F., Moreno, H., Figueroa, O., Muñoz Bravo, J., Vásquez, R.T., Stern, C.R., 2007. Andean magmatism. In: Moreno, T., Gibbons, W. (Eds.), The Geology of Chile. The Geological Society of London.

Parfitt, R.L., Clayden, B., 1991. Andisols - the development of a new order in soil taxonomy. Geoderma 49, 181–198.

Petit-Breuilh, M., Lobato, J., 1994. Análisis comparativo de la cronología eruptiva histórica de los volcanes Llaima y Villarrica (38°–39° L.S.). Congresso Geològico Chileno, pp. 366–370.

Plug, L.J., Gosse, J.C., McIntosh, J.J., Bigley, R., 2007. Attenuation of cosmic ray flux in temperate forest. J. Geophys. Res. Earth Surf. 112.

Porder, S., Chadwick, O.A., 2009. Climate and soil-age constraints on nutrient uplift and retention by plants. Ecology 90, 623–636.

Porder, S., Vitousek, P.M., Chadwick, O.A., Chamberlain, C.P., Hilley, G.E., 2007. Uplift, erosion, and phosphorus limitation in terrestrial ecosystems. Ecosystems 10, 159–171.

Quirk, J., Beerling, D.J., Banwart, S.A., Kakonyi, G., Romero-Gonzalez, M.E., Leake, J.R., 2012. Evolution of trees and mycorrhizal fungi intensifies silicate mineral weathering. Biol. Lett. 8, 1006–1011.

Quirk, J., Andrews, M.Y., Leake, J.R., Banwart, S.A., Beerling, D.J., 2014. Ectomycorrhizal fungi and past high CO_2 atmospheres enhance mineral weathering through increased below-ground carbon-energy fluxes. Biol. Lett. 10.

Richter, D.D., Markewitz, D., 1995. How deep is soil? Bioscience 45, 600–609.

Riebe, C.S., Granger, D.E., 2013. Quantifying effects of deep and near-surface chemical erosion on cosmogenic nuclides in soils, saprolite, and sediment. Earth Surf. Process. Landf. 38, 523–533.

Riebe, C.S., Kirchner, J.W., Granger, D.E., Finkel, R.C., 2001. Strong tectonic and weak climatic control of long-term chemical weathering rates. Geology 29, 511–514.

Riebe, C.S., Kirchner, J.W., Finkel, R.C., 2003. Long-term rates of chemical weathering and physical erosion from cosmogenic nuclides and geochemical mass balance. Geochim. Cosmochim. Acta 67, 4411–4427.

Riebe, C.S., Kirchner, J.W., Finkel, R.C., 2004. Erosional and climatic effects on long-term chemical weathering rates in granitic landscapes spanning diverse climate regimes. Earth Planet. Sci. Lett. 224, 547–562.

Riebe, C.S., Hahm, W.J., Brantley, S.L., 2017. Controls on deep critical zone architecture: a historical review and four testable hypotheses. Earth Surf. Process. Landf. 42, 128–156.

Riquelme, R., Martinod, J., Hérail, G., Darrozes, J., Charrier, R., 2003. A geomorphological approach to determining the Neogene to Recent tectonic deformation in the Coastal Cordillera of northern Chile (Atacama). Tectonophysics 361, 255–275.

Rundel, P.W., Weisser, P.J., 1975. La Campana, a new national park in central Chile. Biol. Conserv. 8, 35–46.

Rundel, P.W., Villagra, P., Dillon, M., Roig-Junent, S., 2007. Arid and semi-arid ecosystems. In: Veblen, T., Young, K., Orme, A. (Eds.), The Physical Geography of South America. Oxford Univ. Press, New York, pp. 158–183.

Schaller, M., Ehlers, T.A., Lang, K.A.H., Schmid, M., Fuentes-Espoz, J.P., 2018. Addressing the contribution of climate and vegetation cover on hillslope denudation, Chilean Coastal Cordillera (26°–38°S). Earth Planet. Sci. Lett. 489, 111–122.

Scholten, T., Felix-Henningsen, P., Schotte, M., 1997. Geology, soils and saprolites of the Swaziland Middleveld. Soil Technol. 11, 229–246.

Schoonejans, J., Vanacker, V., Opfergelt, S., Ameijeiras-Mariño, Y., Christl, M., 2016. Kinetically limited weathering at low denudation rates in semiarid climatic conditions. J. Geophys. Res. Earth 121, 336–350.

Schutz, K., Kandeler, E., Nagel, P., Scheu, S., Ruess, L., 2010. Functional microbial community response to nutrient pulses by artificial groundwater recharge practice in surface soils and subsoils. FEMS Microbiol. Ecol. 72, 445–455.

Schwertmann, U., 1964. Differenzierung der Eisenoxide des Bodens durch Extraktion mit Ammoniumoxalat-Lösung. J. Plant Nutr. Soil Sci. 105, 194–202.

Schwertmann, U., 1985. The effect of pedogenic environments on iron oxide minerals. In: Advances in Soil Science. Springer, New York, pp. 171–200.

Scott, K.M., Pain, C.F., 2008. Regolith Science. Springer.

SERNAGEOMIN, 2003. Mapa Geológico de Chile: versión digital. Servicio Nacional de Geología y Minería, Publicación Geológica Digital, No. 4, Santiago.

Smits, M.M., Bonneville, S., Benning, L.G., Banwart, S.A., Leake, J.R., 2012. Plant-driven weathering of apatite - the role of an ectomycorrhizal fungus. Geobiology 10, 445–456.

Staff, S.S., 1999. Soil Taxonomy. A Basic System of Soil Classification for Making and Interpreting Soil Surveys. USDA Natural Resources Conservation Service, Washington.

Starke, E., Ehlers, T.A., Schaller, M., 2017. Tectonic and climatic controls on the spatial distribution of denudation rates in northern Chile (18°S to 23°S) determined from cosmogenic nuclides. J. Geophys. Res. Earth 122.

Streckeisen, A.L., LeMaitre, R.W., 1979. Chemical approximation to modal QAPF classification of the igneous rocks. N. Jb. Mineral. 136, 169–206.

Tamm, O., 1922. Method for the estimation of the inorganic components of the gel-complex in soils. Medd Statens Skogsförsöksanst. 19, 385–404.

Tchakerian, V., Pease, P., 2015. The critical zone in desert. Environments 449–472.

Uhlig, D., Schuessler, J.A., Bouchez, J.L., Dixon, J., von Blanckenburg, F., 2017. Quantifying nutrient uptake as driver of rock weathering in forest ecosystems by magnesium stable isotopes. Biogeosci. Discuss. 1–28.

Vázquez, M., Ramírez, S., Morata, D., Reich, M., Braun, J.-J., Carretier, S., 2016. Regolith production and chemical weathering of granitic rocks in central Chile. Chem. Geol.

446, 87–98.

von Blanckenburg, F., 2005. The control mechanisms of erosion and weathering at basin scale from cosmogenic nuclides in river sediment. Earth Planet. Sci. Lett. 237, 462–479.

von Blanckenburg, F., O'Nions, R.K., Belshaw, N.S., Gibb, A., Hein, J.R., 1996. Global distribution of beryllium isotopes in deep ocean water as derived from Fe-Mn crusts. Earth Planet. Sci. Lett. 141, 213–226.

Wada, K., Dixon, J.B., 1989. Allophane and imogolite. In: Weed, S.B. (Ed.), Minerals in Soil Environments, pp. 1051–1087.

White, A.F., 2002. Determining mineral weathering rates based on solid and solute weathering gradients and velocities: application to biotite weathering in saprolites. Chem. Geol. 190, 69–89.

White, A.F., Blum, A.E., Schulz, M.S., Vivit, D.V., Stonestrom, D.A., Larsen, M., Murphy,

S.F., Eberl, D., 1998. Chemical weathering in a tropical watershed, Luquillo Mountains, Puerto Rico: I. Long-term versus short-term weathering fluxes. Geochim. Cosmochim. Acta 62, 209–226.

Wilcke, W., Velescu, A., Leimer, S., Bigalke, M., Boy, J., Valarezo, C., 2017. Biological versus geochemical control and environmental change drivers of the base metal budgets of a tropical montane forest in Ecuador during 15 years. Biogeochemistry 1–23.

Will, C., Thurmer, A., Wollherr, A., Nacke, H., Herold, N., Schrumpf, M., Gutknecht, J., Wubet, T., Buscot, F., Daniel, R., 2010. Horizon-specific bacterial community composition of German grassland soils, as revealed by pyrosequencing-based analysis of 16S rRNA genes. Appl. Environ. Microbiol. 76, 6751–6759.

Zvyagintsev, D., 1994. Vertical distribution of microbial communities in soils. In: Ritz, K., Dighton, J., Giller, K. (Eds.), Beyond the Biomass. Wiley, West Sussex, UK, pp. 29–37.